Rep. Prog. Phys. **71** (2008) 016101 (23pp) doi:10.1088/0034-4885/71/1/016101

Atomic force microscopy and spectroscopy

Yongho Seo[1] **and Wonho Jhe**[2]

[1] Faculty of Nanotechnology & Advanced Material Engineering and Institute of Fundamental Physics, Sejong University, Seoul 143-747, Korea
[2] Center for Nano Liquid and Department of Physics and Astronomy, Seoul National University, Seoul 151-747, Korea

E-mail: whjhe@snu.ac.kr

Received 4 July 2007, in final form 25 September 2007
Published 17 December 2007
Online at stacks.iop.org/RoPP/71/016101

Abstract
Since it was invented by Binnig *et al* in 1986, atomic force microscopy (AFM) has played a crucial role in nano-scale science and technology. AFM is a microscopic technique imaging a surface topography by using attractive and repulsive interaction forces between a few atoms attached at a tip on a cantilever and a sample. In the case of attractive forces, there are three main contributions causing AFM. These are short-range chemical force, van der Waals force and electrostatic force. As the effective ranges of these forces are different, one of them is dominant depending on distance. Atomic force spectroscopy is the force-versus-distance measurement when using AFM. The atomic force can be detected by cantilever bending caused by a tip–sample interacting force, which is called static AFM. Also, the atomic force can be detected by using the resonant properties of a cantilever, which is called dynamic AFM. Under the on-resonance condition, the frequency, amplitude or phase of the cantilever will be shifted by the interaction force. While the force can be estimated in static AFM, for dynamic AFM it requires complicated formalism to evaluate the force from measured amplitude, phase or frequency data. Recently developed techniques for ultra-high resolution imaging unveil sub-atomic features of the sample, which are facilitated by low temperature, ultra-high vacuum environments together with a stiff cantilever. In this study, progress related to theoretical and experimental imaging and force spectroscopy will be discussed.

(Some figures in this article are in colour only in the electronic version)

This article was invited by Professor J Weiner.

Contents

1. Introduction

Since its development in 1986 by Binnig [1, 2], many experimental studies on nano-scale phenomena have utilized atomic force microscopy (AFM) to image the atomic topography and measure interacting forces [3–5]. AFM has been employed in a variety of research fields including physics, chemistry, biology and engineering. In order to measure the force or potential energy between a small tip and a sample, a tiny probe called a cantilever is employed. The cantilever provides a force sensor and a force actuator. By pushing the cantilever to the sample, its topographic height can be measured, and the interacting force between the tip attached to the cantilever and the sample can be measured by pulling it. There are various methods for detecting the motion of the cantilever with nanometre scale accuracy. These include tunneling current measurement [2], optical deflection technique [6], fiber interferometry [7] and piezoresistive methods [8].

At first, Binnig used a gold foil as a cantilever and attached a diamond tip to it [2]. Now cantilevers are made of Si [10], SiO_2 or Si_3N_4 [9] by using a micromachining technique. Figure 1 shows an example of a design of a commercial cantilever. The large holding block is a piece cut from a Si wafer and a tiny cantilever is formed on it. For optical detection of cantilever motion, the back side of the cantilever is supposed to be reflective. It is coated with a metallic film. A tip of a few μm length facing down is attached to the cantilever. The typical dimensions of the cantilever are $W \simeq 30\,\mu\text{m}, t \simeq 1\,\mu\text{m}$ and $L \simeq 100\,\mu\text{m}$.

When a tip is close to a sample, it experiences an attractive force. Then, the force becomes repulsive at a certain point. If the tip–sample distance is closer than the switching point, the tip is in contact with the sample. In contrast, the terminology 'non-contact' means that the tip is away from the contact regime. By pushing the tip close to the sample and pulling back, one can measure the cantilever deflection, which is supposed to be proportional to the interacting force between the tip and the sample. This is the basic principle of static AFM where the force can be estimated by using Hooke's law.

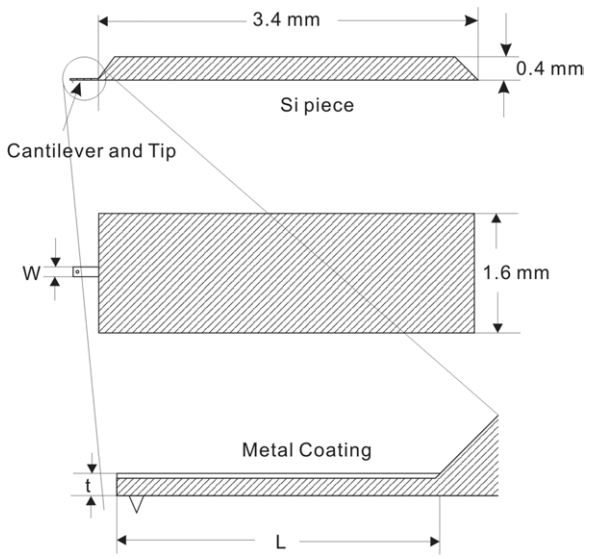

Figure 1. Example of the design of a commercial cantilever. The large holding block is a Si piece and a tiny cantilever ~100 μm long is attached to it. A tip ~10 μm long facing down is attached to the cantilever. Typically, the back side of the cantilever is coated with a metallic film.

On the other hand, the cantilever can be vibrated with resonance frequency and topographic information. Its force can be estimated from the change of vibrating amplitude, phase or resonance frequency. This is the so-called dynamic AFM. Due to its simplicity, studies in a variety of fields including molecular or biological samples have been performed using the static AFM method [11]. However, the principle of dynamic AFM is complicated, and interpreting it is also challenging. Dynamic AFM can be classified into AM-AFM (amplitude modulation AFM) and FM-AFM (frequency modulation AFM). The AM-AFM measures the amplitude change of cantilever vibration excited by an external force with a constant frequency, whereas the FM-AFM measures its resonance frequency change excited by a positive feedback oscillation. There have been many efforts to extract the force information from experimental dynamic AFM data. Perturbation theory, Fourier expansion, variational methods and inversion procedures were also developed to find the relationship between frequency shifts and tip–sample interaction.

To improve the force sensitivity or the signal to noise (S/N) ratio, theoretical and experimental parameter studies on the amplitude and stiffness of the cantilever have been performed. For high resolution measurements, very small vibration amplitude (~1 Å) and high stiffness ($\sim 10^3\,\text{N m}^{-1}$) were suggested [5, 12–14]. A special sensor which satisfies this condition is the quartz crystal tuning fork (TF). Since Karrai and Grober employed it for the near-field scanning optical microscope [15], the tuning fork has become a very promising force sensor for almost all types of scanning probe microscopies including electrostatic [16] and magnetic force microscopy [17]. In this report, the general principles of AM- and FM-AFM, force spectroscopy, imaging of atoms and recent experimental techniques for atomic resolution imaging and force measurement are discussed.

2. Interacting forces

With AFM, one can measure the force between atoms at the tip and the sample which are located as close as 0.1–100 nm. The forces can be classified into attractive and repulsive forces. For attractive forces, van der Waals (vdW) interaction, electrostatic force and chemical force are included. The chemical forces are described by many different theoretical models. Among them, we can mention Morse potential [18], Stillinger–Weber potential and Tersoff potential [5]. The repulsive forces can be considered as hard sphere repulsion, Pauli-exclusion interaction and electron–electron Coulomb interaction. In general, the repulsive forces are very short-range forces and have an exponential decaying or inverse power law with high-order distance dependence.

2.1. van der Waals interactions

The van der Waals interaction is based on the Coulomb interaction between electrically neutral atoms which are locally charged by thermal or zero-point quantum fluctuations [19]. It is well known that the vdW potential between two atoms has a distance dependence of $\sim z^{-6}$. In the case of AFM measurements, however, there are several hundred atoms at a tip and sample, and the resultant force should be calculated from a vector sum of vdW forces between them. The vdW interaction between macroscopic samples was calculated by Hamaker [20]. Hamaker's approach does not consider the retardation effect due to the finite speed of light. It is applicable for a sample and tip of ∼10 nm scale [5]. For a spherical tip with radius R and a flat sample, the vdW potential V_{vdW} and force F_{vdW} are given by [18]

$$V_{\mathrm{vdW}} = -\frac{A_{\mathrm{H}} R}{6z}, \qquad F_{\mathrm{vdW}} = -\frac{A_{\mathrm{H}} R}{6z^2}, \tag{1}$$

where z is the closest distance between the tip and the sample and A_{H} is the Hamaker constant. The Hamaker constant is determined by the physical properties of materials such as atomic polarizability and the density of the tip and the sample. Typically, A_{H} is in the order of 1 eV for solids. Depending on the shape of the tip and the sample V_{vdW} can have different power laws. In the case of conical and pyramidal tips, V_{vdW} is estimated as $\simeq \ln z$ [21]. For a tip with radius $R = 10$ nm and distance $z = 1$ nm, the vdW potential is $\simeq -1.6$ eV and the corresponding force is ≃0.3 nN. This amount of force is significant for nanometre scale and the vdW force provides a major contribution to AFM topographic measurement [5]. In order to reduce the vdW interaction, one can perform the AFM measurement by immersing the tip and sample in water [22]. Then, the van der Waals forces exerted by the water molecules cancel out the force between the tip and sample.

2.2. Electrostatic force

The electrostatic force is generated between a charged or conductive tip and sample which have potential difference U. For a tip–sample distance z smaller than the tip radius R, the electrostatic force F_{el} is given by [23–25]

$$F_{\mathrm{el}}(z) = -\frac{\pi \epsilon_0 R U^2}{z}, \tag{2}$$

where ϵ_0 is the dielectric constant. As F_{el} has z^{-1} power law dependence, the electrostatic force is a relatively long-range force compared with the vdW force. For example, in typical experimental conditions, the $U \simeq 1$ V, $R \simeq 100$ nm and $z = 1$ nm, the electrostatic force F_{el} amounts to ≃3 nN [5].

The electrostatic force is not limited, but ferroelectric or charged semiconducting samples experience the electrostatic force. Moreover, ionic crystals like KBr, LiF, NaCl and MgO also exert an electrostatic force to the tip on the atomic scale [26–28]. The electrostatic force exerted by ionic crystals provides a short-range force because at a long distance from the surface, neighboring anions and cations cancel each other's electrostatic forces [5].

2.3. Chemical force

When two or more atoms come together to form a molecule, the force that tightly binds the atoms is called a chemical force [18]. For covalent bonds, the force is referred to as a covalent force. The covalent bonds have directionality depending on atomic location and valency. Covalent forces are short range (0.1–0.2 nm) [18]. Their bonding energies are 100–300 $k_{\mathrm{B}}T$ per bond and these forces are roughly 3–9 nN.

The chemical force can be treated on the basis of quantum mechanics [5]. The chemical bonding energy is described by the Morse potential V_{Morse} [5, 18],

$$V_{\mathrm{Morse}} = -E_{\mathrm{bond}}(2\mathrm{e}^{-\kappa(z-\sigma)} - \mathrm{e}^{-2\kappa(z-\sigma)}), \tag{3}$$

where E_{bond} is bonding energy, σ equilibrium distance and $1/\kappa$ decay length. The Morse potential is induced by approximation of the covalent bonding interaction.

2.4. Capillary force

A hydrophilic surface adsorbs water molecules in ambient conditions and a water layer forms on the surface. When a tip is close to the water layer, a liquid bridge called a meniscus is formed between the tip and the sample. This meniscus causes an attractive force (called capillary force) between the tip and the sample. The basis of the capillary force is the vdW forces among the water molecules and atoms at the tip and the sample [29, 30].

Recently, Jhe's group reported on the formation and manipulation of a nanometre scale meniscus of condensed water molecules that form between the tip and the sample [31]. They used a trident-shape quartz tuning fork as a force sensor [32]. An unusual stepwise decrease in the force gradient associated with a thin water bridge formed between the tip–sample gap was observed while the tip retracted. The stepwise force gradient change showed regularity in step heights (0.5 N m^{-1}) and plateau lengths (1 nm). Such quantized elasticity was explained as an atomic-scale stick slip at the tip–water interface. A thermodynamic-instability-induced rupture of the water meniscus (5 nm long and 2.6 nm wide) was also found. This study opened up a research field for a nanometric aqueous column [31].

2.5. Repulsive force

Basically, the repulsive force between the tip and the sample is referred to as the Pauli exclusion or ionic repulsion [19]. As an atom approaches another atom, the electronic wave function will be overlapped and a very strong repulsion will be generated by either Coulomb force or Pauli exclusion [19]. Generally, this repulsion force is short range. For instance, in Lennard–Jones (LJ) potential

$$V_{\mathrm{LJ}} = -4\epsilon\left(\frac{\sigma^6}{z^6} - \frac{\sigma^{12}}{z^{12}}\right), \tag{4}$$

where ϵ is the depth of the potential well, σ is the distance at which the force is zero. The z^{-6} distance dependence comes from the van der Waals attractive interaction and

z^{-12} is given by the repulsive force between two atoms [19]. The LJ potential was derived from approximation of two atom interaction. In the case of many atomic interactions, the Hamaker approach integrates the whole vector forces applied, and the z^{-12} dependence will be modified depending on the shape of the tip. If the contact area between the tip and the sample is large and tens or hundreds of atoms are involved in the contact, the repulsive force can be considered a mechanical or elastic force due to physical deformation [4]. The models based on the elasticity and adhesion include Hertz, Johnson–Kendall–Roberts (JKR) and Derjaguin–Muller–Toporoz (DMT) [3, 4].

2.6. Atomic resolution

Since the Si 7 × 7 reconstruction on a Si(1 1 1) surface was imaged using a scanning tunneling microscope (STM) invented in 1982 by Binnig and Rohrer [33, 34], atomic resolution imaging has been obtained by STM routinely. In the case of AFM, Giessibl showed the Si 7 × 7 using UHV condition AFM in 1995 [35]. He used a modified cantilever beam and measured the force gradient employing the frequency modulation technique. The Si 7 × 7 structure was imaged in a non-contact mode with atomic resolution 6 Å lateral, 0.1 Å vertical.

On the other hand, in contact mode AFM, there is controversy related to whether or not the true atomic resolution can be obtained [36]. For example, atomic resolution for layered materials was reported [37], but the images rarely showed any individual surface defects which were routinely observed by STM. In particular, atomic-scale patterns persist even at large forces of up to 100 nN. The contact area is estimated to be 100 Å, which indicates that the images obtained may represent collective interactions between several atoms in the tip and the sample [32]. It is also difficult to obtain true atomic resolution in ambient conditions by using non-contact AFM, due to air drift and sound noise, as well as surface adsorbates.

Giessibl obtained an ultra high resolution (sub-atomic scale) image of Si 7 × 7 structure by using a quartz tuning fork rather than conventional cantilevers [35]. The quartz tuning fork has high stiffness 2 or 3 orders of magnitude higher than that of the cantilever. Also, Jhe's group obtained an atomic resolution by using non-contact AFM with a quartz tuning fork in ambient conditions [32]. They employed a high stiffness, trident-shaped quartz crystal tuning fork oscillating at 1 MHz with a high spring constant of 4×10^4 N m^{-1}. The high stiffness sensor allowed true atomic resolution of a cleaved mica surface in air.

In general, the atomic resolution is provided by short-range interactions [4]. The vdW interaction is a long range and collective force including many atoms at the tip and in the sample. Rather than vdW interaction, the chemical interaction of covalent crystal or electrostatic force given by ions of the ionic crystal is supposed to be dominant to achieve atomic resolution.

For semiconductor surfaces, the most probable source providing atomic resolution is the covalent bonding interaction (chemical force) [4]. For both the semiconductor (Si) surface and the Si tip, there are uncoordinated dangling bonds, through which the atoms in the tip and the sample may have strong attractive interaction to form a covalent bonding. This behavior is purely a quantum mechanical phenomenon and completely different from vdW interaction.

3. Static atomic force microscopy and spectroscopy

3.1. Static atomic force microscopy

While the STM uses a tunneling current between a metallic tip and a sample to control the distance between the sample and the tip, the static AFM is operated by measuring a repulsive force between the sample and the tip. The repulsive atomic force includes electronic Coulomb repulsion or Pauli-exclusion force. For AFM, the sample and the tip are not necessarily metallic, differently from STM. When Binnig *et al* [1, 2] invented the AFM, they employed the tunneling current measurement technique, similarly to STM, to measure the deflection of the metallic cantilever. In addition to the cantilever, another metallic tip was placed close to the back side of the cantilever, and the tunneling current from the tip to the cantilever was measured. Besides the tunneling current method, capacitance measurement, optical deflection technique, optical fiber interferometry and piezoelectric (or piezoresistive) [8, 38–40] techniques were developed for detecting the cantilever bending motion. Among them, the optical deflection technique has been considered the most reliable and sensitive method for general AFM.

Figure 2 shows a schematic of the optical deflection technique. A laser beam from a laser diode (LD) is focused on the end of the cantilever, and the reflected beam is aligned at the center of the position sensitive photo diode (PSPD). The PSPD has a quadrant shape with four independent photo-diodes separated with ∼100 μm gap. When the tip experiences an attractive (repulsive) force, the cantilever will be bent toward

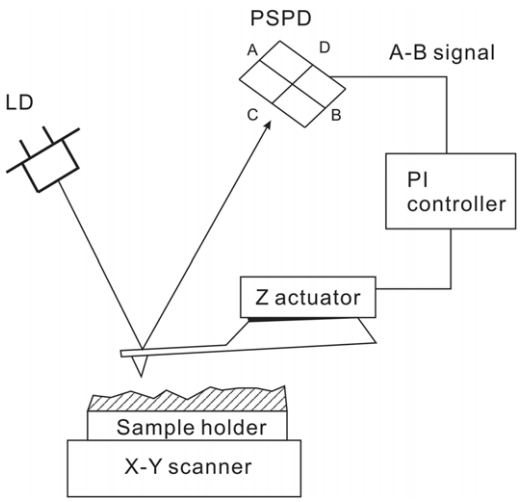

Figure 2. Optical deflection technique. A laser beam from a LD is focused at the end of the cantilever, and a reflected beam is aligned at the center of the PSPD. When the cantilever bends, the A–B signal of the PSPD is changed and fed to the PI controller to control the height of the cantilever through the Z-actuator.

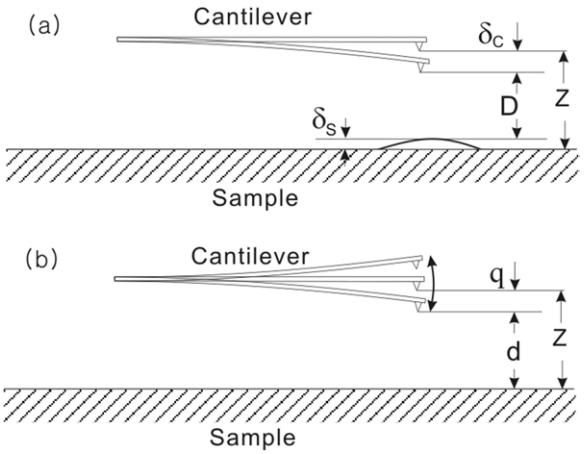

Figure 3. Tip–sample distance parameters for (*a*) static and (*b*) dynamic AFM. (*a*) z is defined as the distance between the sample and the tip assuming no interaction between them exists. D is the real tip–sample distance. δ_c and δ_s are the displacements of the cantilever and the sample due to the tip–sample interaction, respectively. (*b*) z is defined as an average distance between the tip and the sample, d the minimum distance and q the instant displacement from z of the cantilever when the cantilever is oscillated by an external force.

(away from) the sample surface. The face of the PSPD is oriented toward the bounced beam. When the cantilever is bent toward (away from) the surface, the beam path is shifted to the upper (lower) two photo-diodes. The beam path shift causes the intensity difference between the upper and lower photo-diodes which is called the A–B signal. The A–B signal is fed to a proportion-integration (PI) controller to control the bending angle of the cantilever through a Z-actuator made by a piezo-actuator. In the past, the PI controller circuit was produced by analog electronics. Now, it is operated by a DSP chip set or a stand-alone computer (so-called real-time module) for digital control.

The static AFM was named to be distinguished from the dynamic AFM. While in the former the cantilever remains static, in the latter the cantilever is vibrated with its resonance frequency. In static AFM, the bending of the cantilever is only observable and its bending force can be calculated by Hooke's law. The cantilever can be approximated as a spring with damping. Ignoring its transient behavior, the position shift of the cantilever end is equal to the force divided by its spring constant k. Typically, the spring constant k of a micro-machined cantilever is designed to be 0.1–10 N m^{-1}, depending on its particular experimental purpose. The free position z in figure 3(*a*) is defined as the distance between the sample and the cantilever assuming no interacting force between them exists. If the tip–sample distance is considerable, the interaction can be ignored, and z can be estimated from the applied voltage on the Z-actuator by using calibration data. So z is the only controllable parameter in this system, and it is called the displacement rather than the distance. Due to the tip–sample interaction not only the cantilever but also the sample is subject to deformation. δ_c is the vertical position change of the tip from the original point z which can be expected in non-interacting conditions. δ_s implies the inflation (or deflation) of the sample due to the interaction. Finally, D is the real tip–sample distance, $D = z - \delta_c - \delta_s$. Typically, the spring constant of cantilever k is much smaller than that of the sample and δ_s can be ignored for common solid samples.

3.2. Force spectroscopy using static AFM

Force spectroscopy is a technique to measure a local force acting on the tip exerted by a sample with spatial resolution on the nanometre scale. While AFM imaging is performed by scanning the sample (or tip) in the XY-direction, force spectroscopy is done by approaching and retracting the tip (or sample) in the Z-direction. The force–distance curve is a plot of the tip–sample interaction force versus the tip–sample distance. In order to obtain the force–distance curve, the tip (or the sample) is ramped along the vertical axis (Z-axis) and the cantilever deflection δ_c is measured. The cantilever bending force is given by Hooke's law:

$$F_c = -k\delta_c, \tag{5}$$

where k is the spring constant of the cantilever and F_c the elastic force of the cantilever. The AFM force–distance curve is given by balancing two contributing forces. These are the tip–sample interaction force $F(D)$ and the elastic force of the cantilever F_c. By using the graphical interpretation shown in figure 4, one can understand the resulting force–displacement curve. In figure 4(*a*) the curve $F(D)$ shows the typical shape of the tip–sample interacting force as a function of the distance D, which consists of long range attractive (e.g. van der Waals force) and short-range repulsive forces (e.g. Lennard–Jones, or Morse force), as discussed in section 2. Ignoring δ_s ($D = z - \delta_c$), equation (5) can be modified as a function of D;

$$F_c(D) = k \cdot (D - z). \tag{6}$$

The lines 1–4 show F_c as a function of D. In an equilibrium state, the $F(D)$ should be equal to F_c and that point is given by the intersection (α, β, γ, δ) of two lines. At the intersection point β for example, the D value is the real distance between the tip and the sample. The controllable (or measurable) value z is given by the intersection between the line 2 and the x-axis, and the δ_c is determined by the difference between D_β and z_β as depicted in the graph. The value we want to know is the force between the tip and sample which is equal to $F_c = k\delta_c$.

In figure 4(*b*) the resulting force–displacement curve is illustrated. At each distance, the cantilever is bent until the elastic force of the cantilever becomes equal to the tip–sample interaction force. In this way, the system reaches equilibrium. When the tip is far from the sample (1), $F(D)$ is close to zero. At the intersecting point α in figure 4(*a*), δ_c is also close to zero, as indicated in (*b*). As the tip approaches the sample, the gap between D and z will grow, monotonically. Because z is larger than D, δ_c and F_c are negative numbers, there is an attractive force. At point β, an abrupt change occurs which is called *jump-to-contact*. The jump-to-contact means that the cantilever bent by the attractive force jumps to the surface of the sample. At γ, the F_c becomes a positive value meaning

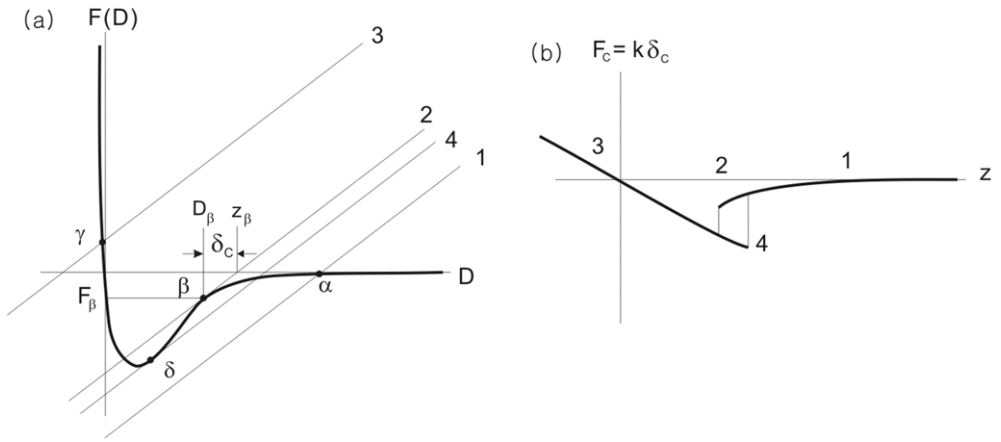

Figure 4. (*a*) The curve $F(D)$ shows the typical shape of the tip-sample interacting force. The lines 1–4 show F_c as a function of D. In an equilibrium state, the $F(D)$ should be equal to F_c and that point is given by the intersection (α, β, γ, δ) of two lines. At the intersection point β, F_β is the interacting force, D_β is the tip-sample distance and the δ_c is the cantilever bending distance. (*b*) Interacting force as a function of distance. The interacting force is equal to F_c which bends the cantilever. This force is determined by δ_c depicted in panel (*a*).

repulsive force. Because the repulsive force $F(D)$ is very stiff, in the region near 3 in figure 4(*b*) the force curve is close to a straight line. In a retracting process, the cantilever will follow the trace from 3 to 4 producing a hysteresis loop. At point δ, there is another abrupt change called *jump-off-contact*, which means that the tip is separated from the sample surface, all of a sudden. The curves in figure 4(*b*) are called force–displacement curves *hysteresis* [3]. On the other hand, in the case of a stiff cantilever (k is larger) the slopes of lines 1, 2, 3 and 4 are steeper. Then, abrupt change at β and δ will not occur and no hysteresis will occur.

Hao *et al* suggested an analytical expression for force–displacement curves [41]. The total potential V_{tot} is the sum of three potentials: $V_{tot} = V_{ts}(D)+V_c(\delta_c)+V_s(\delta_s)$. Here, $V_{ts}(D)$ is the interaction potential between the tip and the sample, e.g. the Lennard–Jones potential. $V_c(\delta_c)$ and $V_s(\delta_s)$ are Hooke's elastic potentials of the cantilever and the sample surface, respectively. The Hooke's elastic potentials are described by

$$V_c(\delta_c) = \frac{1}{2}k_c{\delta_c}^2,$$
$$V_s(\delta_s) = \frac{1}{2}k_s{\delta_s}^2, \tag{7}$$

where k_c and k_s are the cantilever and sample spring constants. Typically, the attractive force $F(D) = -\partial V_{ts}/\partial D$ between the tip and the sample can be written as a power law form:

$$F(D) = -\frac{C}{D^n}, \tag{8}$$

where C and n are parameters depending on the specific shape and material properties of the tip and the sample. As equation (8) takes into account the attractive part of the interaction, it is valid for non-contact regions. Here, we want to find the relationship between z and δ_c from equation (8). Due to the static equilibrium condition, $k_s\delta_s = k_c\delta_c$, that is,

$$\delta_s = \frac{k_c}{k_s}\delta_c. \tag{9}$$

The above equation shows that one can determine δ_s from δ_c, if k_c and k_s are known. In a state of equilibrium the forces are balanced:

$$\frac{\partial V_{tot}}{\partial \delta_s} = \frac{\partial V_{tot}}{\partial \delta_c} = 0. \tag{10}$$

Since $\partial V_{cs}/\partial\delta_s = -\partial V_{cs}/\partial D$, because $D = z - \delta_c - \delta_s$, we obtain

$$k_c\delta_c = \frac{C}{(z-\delta_c-\delta_s)^n} = \frac{C}{(z-\beta\delta_c)^n}, \tag{11}$$

where $\beta = (1 + k_c/k_s)$. In equation (11), δ_c is a measurable quantity by using the cantilever calibration process and z is a controllable quantity. Therefore, the potential parameters C and n can be estimated by using the experimental data of δ_c and z.

For the system to be in stable equilibrium, $\partial^2 V_{tot}/\partial{\delta_c}^2$ should be larger than zero:

$$\frac{k_c}{\beta} > \frac{nC}{(z-\beta\delta_c)^{n+1}}, \tag{12}$$

where k_c/β is referred to as the effective elastic constant. If the force gradient given by the right term in equation (12) is larger than the effective elastic constant, the cantilever becomes unstable and jump-to-contact occurs. From equations (11) and (12) the cantilever deflection at jump-to-contact $(\delta_c)_{jtc}$ and the tip–sample distance D_{jtc} can be determined:

$$(\delta_c)_{jtc} = \left(\frac{C}{(n\beta)^n k_c}\right)^{1/(n+1)}, \tag{13}$$
$$D_{jtc} = \beta n(\delta_c)_{jtc}. \tag{14}$$

By using equation (14), C and β can be estimated from $(\delta_c)_{jtc}$ and D_{jtc} measured experimentally.

For instance, let us assume a tip–sample force $F(D) = -C_2/D^2 + C_3/D^3$, in which the attractive part represents a van der Waals interaction between a sphere (tip) and a flat surface (sample). Typically, these parameters are $C_2 \simeq 10^{-28}\,\mathrm{Nm}^2$ and $C_3 \simeq 10^{-38}\,\mathrm{Nm}^3$ [42]. Figure 5(*a*) shows the force curve of our trial force. When the cantilever tip approaches the

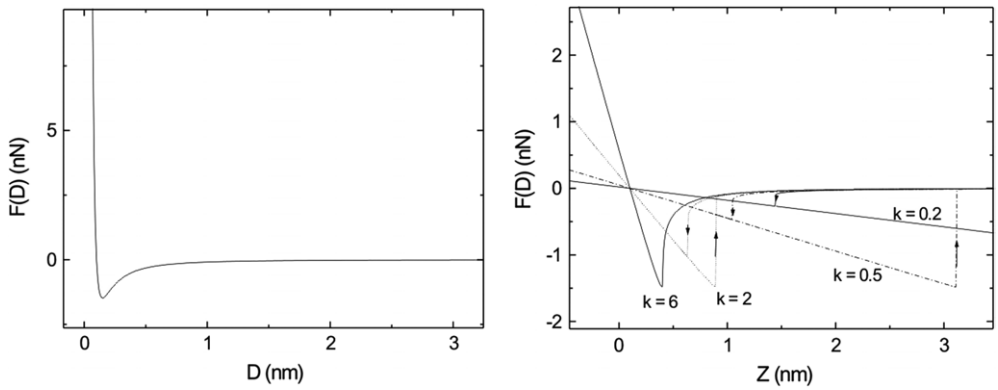

Figure 5. (*a*) The force curve of a van der Waals interaction $F(D) = -C_2/D^2 + C_3/D^3$. (*b*) For $k_c = 0.2$, 0.5, 2 and 6 N m^{-1}, δ_c is calculated numerically as a function of z, and the tip–sample interacting force $F_{eq}(D)$ in equilibrium state, is calculated by $F_{eq}(D) = -k_c\delta_c$.

sample, the cantilever displacement δ_c can be estimated by equation (10) assuming $\delta_s = 0$ ($D = z - \delta_c$);

$$k_c\delta_c - \frac{10^{-28}}{(z-\delta_c)^2} + \frac{10^{-38}}{(z-\delta_c)^3} = 0. \qquad (15)$$

For $k_c = 0.2$, 0.5, 2 and 6 N m^{-1}, δ_c is calculated numerically as a function of z. Finally, the tip–sample interacting force $F_{eq}(D)$ in an equilibrium state, is simply calculated by $F_{eq}(D) = -k_c\delta_c$, as shown in figure 5(*b*). In the case of a stiff cantilever ($k_c = 6$), the $F_{eq}(D)$ is single valued as a function of z. However, in the case of a soft cantilever ($k_c \leqslant 2$), δ_c has three solutions in equation (15) in between the jump-to-contact and the jump-off-contact points. When the tip is far from the sample, δ_c is close to zero. As it approaches the sample beyond the jump-off-contact point, δ_c has three possible values, among which the smallest variation value is chosen. At the jump-to-contact point, the δ_c changes abruptly, thereby ending the three valued state. After the jump-to-contact point, $F_{eq}(D)$ increases almost linearly, changing its polarity as shown in figure 5(*b*). The polarity change shows the change from attractive to repulsive interacting force. During the retracting process, the tip follows the same trace as the approaching trace, initially. However, at the beginning of the three valued regions, the cantilever may choose the smooth change causing hysteresis. Hysteresis will end at the jump-off-contact point. As shown in figure 5(*b*), as the cantilever is softer, it creates larger hysteresis. The relationship between hysteresis and the spring constant is shown in figure 6. The $(\delta_c)_{jtc}$ and $(\delta_c)_{joc}$ are calculated from $\partial V_{tot}/\partial\delta_c = 0$ and $\partial^2 V_{tot}/\partial{\delta_c}^2 = 0$. As shown in figure 5(*b*), while a low stiffness cantilever ($k \simeq 0$) has large hysteresis, for stiff cantilever $k > 6$ N m^{-1} no hysteresis appears.

As a result, a low stiffness cantilever has large bending and high sensitivity as a force sensor, but it causes hysteresis. This is a drawback for the detailed measurement of the tip–sample force. On the other hand, the high stiffness cantilever does not have hysteresis and its bending-distance data resemble the force-distance curve, but its force sensitivity is low.

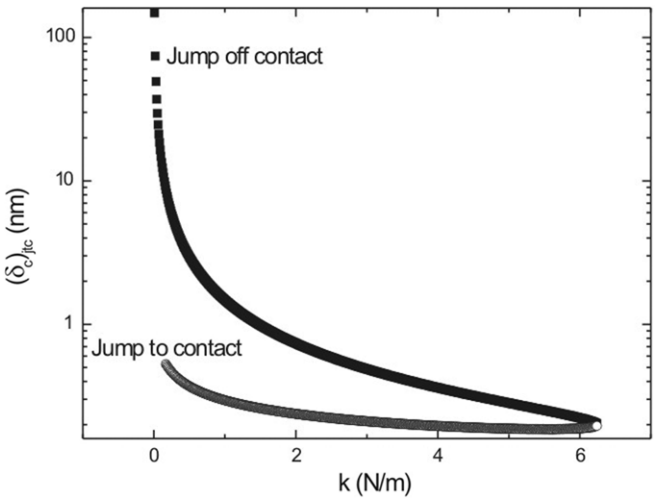

Figure 6. Jump-to-contact and jump-off-contact points versus spring constant k. The $(\delta_c)_{jtc}$ and $(\delta_c)_{joc}$ are calculated from $\partial V_{tot}/\partial\delta_c = 0$ and $\partial^2 V_{tot}/\partial{\delta_c}^2 = 0$.

4. AM atomic force microscopy and spectroscopy

4.1. AM atomic force microscopy

As already mentioned, there are two different types of AFMs, static AFM and dynamic AFM. As the cantilever of static AFM remains static and it scans the sample being contacted to the sample surface, it is also called contact mode AFM (C-AFM). On the other hand, in dynamic AFM the cantilever is vibrated by an actuator at its resonance frequency. As the tip is not physically in contact with the sample, it is also called non-contact AFM (NC-AFM). Martin *et al* [43] developed the NC-AFM in 1987. AFM was operated with very small vibration amplitude (below 1 nm) of the tip and its vibration amplitude measured served as a feedback signal for topographic imaging. After the invention of NC-AFM, Zhong *et al* [44] suggested a modified AFM with large amplitude (>100 nm) of a stiff cantilever ($k = 40$ N m^{-1}). Their AFM is called *tapping mode AFM* (or intermittent C-AFM), implying that the tip is partially influenced by the repulsive force from the sample. It is difficult to discriminate the NC-AFM and tapping AFM. The terminologies are mixed in many commercial AFMs.

In general, C-AFM has been used for force spectroscopy measurement, because of its straightforward interpretation of data analysis. However, if one uses NC-AFM for force spectroscopy, there are crucial advantages; (1) improved force sensitivity, (2) stable force measurements and (3) low thermal offset noise. After it was developed by Martin *et al* [43], the early NC-AFM measured the vibration amplitude of the cantilever to estimate the tip–sample distance. A few years later, a novel technique measuring its resonance frequency shift was developed. The former is called amplitude modulation (AM) AFM, and the latter is called frequency modulation (FM) AFM.

For the excitation of the cantilever, piezoelectric devices like PZT actuators or bimorphs are employed generally. The PZT actuator is located between the cantilever Si chip and the Z-actuator. Typically the PZT actuator is 1 mm thick having ∼1 nm vibration amplitude. With this small excitation, the cantilever vibration can be amplified with ∼100 nm amplitude due to its resonance. The resonance of the cantilever is characterized by three different parameters: (1) amplitude, (2) phase and (3) frequency. Among them, the amplitude of the cantilever can be measured by using the peak-detector or lock-in detection technique while fixing the excitation frequency. When the AFM scans the sample, the amplitude change is measured and used as a feedback signal to control the amplitude. This scheme is called *AM-AFM*, in order to be distinguished from FM-AFM.

Before we discuss the spectroscopy of AM-AFM, let us briefly discuss the principle of the AM-AFM. It is well known that the resonant responses are very sensitive to the external perturbation with the frequency close to the resonance frequency. The cantilever motion q in figure 3(*b*) can be approximated by considering an equation of motion for a 1-dimensional point mass m attached at a spring;

$$m\ddot{q} + kq + \frac{m\omega_0}{Q}\dot{q} = F_{\rm ts} + F_0\cos(\omega t), \tag{16}$$

where F_0 and ω are the amplitude and angular frequency of the sinusoidal driving force exerted by the actuator, respectively. Q is the quality factor of the cantilever and ω_0 is the angular resonance frequency of the cantilever. For the sake of simplicity, the subscript c is omitted in k.

4.1.1. Harmonic approximation. In the absence of tip–sample interaction ($F_{\rm ts} = 0$), equation (16) represents the model for the 1-dim force driven harmonic oscillator with damping. The solution of this second derivative equation is a function of ω. In order to consider asymptotic limits, consider a limiting case: $\omega \simeq 0$ (static limit). In this case, $\ddot{q}$ and $\dot{q}$ are close to zero, and $kq \simeq F_0$. This is the case discussed in the previous section on static AFM. Another limit is $\omega \gg \omega_0$, where the $\ddot{q}$ term dominates and the response is determined by inertia [4]. In this case, the motion of the cantilever is 180° out of phase with the excitation.

The general solution for this model is well known [45]:

$$q = A\cos(\omega t - \phi) + Be^{-\alpha t}\cos(\omega_{\rm r} t + \beta), \tag{17}$$

where $\omega_{\rm r}$ is the resonance angular frequency of the cantilever influenced by the damping effect [46] and ϕ is the phase difference between the driving force and the cantilever motion. The first term is a steady solution and the second term is a transient one. The transient term has exponential decaying time dependence with a time constant $1/\alpha = 2Q/\omega_0$. This time constant could be a significant parameter for a high Q-valued cantilever. For example, in vacuum, the Q-value of the cantilever may be increased by a factor of 10 compared with that in air. The transient term $1/\alpha$ fades out and q will show sinusoidal behavior with an amplitude of A given by the steady term. The amplitude A is dependent on the driving frequency ω;

$$A(\omega) = \frac{F_0/m}{\sqrt{(\omega_0^2 - \omega^2)^2 + (\omega\omega_0/Q)^2}}. \tag{18}$$

The phase ϕ is also a function of ω;

$$\tan\phi = \frac{\omega\omega_0/Q}{\omega_0^2 - \omega^2}. \tag{19}$$

When $\omega = 0$, ω_0 and ∞, $\phi = 0°$, 90° and 180°, respectively. Especially, in case of on-resonance condition ($\omega = \omega_0$), the amplitude A_0 is determined as

$$A_0 \equiv A(\omega = \omega_0) = \frac{QF_0}{k}. \tag{20}$$

The resonance angular frequency with damping $\omega_{\rm r}$ is related to the resonance angular frequency ω_0 without damping;

$$\omega_{\rm r} = \omega_0\sqrt{1 - \frac{1}{2Q^2}}. \tag{21}$$

Now, consider the tip–sample interaction potential as a parabolic potential ($\propto q^2$). Then the force is proportional to q, and the force gradient $\mathrm{d}F_{\rm ts}/\mathrm{d}q$ is constant. The force can be written as

$$F_{\rm ts} = \left(\frac{\mathrm{d}F_{\rm ts}}{\mathrm{d}z}\right)q + \text{const.} \tag{22}$$

By inserting equation (22) into equation (16), one can obtain the same differential equation with a modified spring constant $k_{\rm e}$;

$$k_{\rm e} = k - \frac{\mathrm{d}F_{\rm ts}}{\mathrm{d}z}, \tag{23}$$

which is called the effective spring constant. As a result, the modified resonance frequency is simply

$$\omega' = \sqrt{\frac{k_{\rm e}}{m}} = \sqrt{\frac{k - (\mathrm{d}F_{\rm ts}/\mathrm{d}z)}{m}}. \tag{24}$$

In most cases, a weakly perturbed tip–sample interaction can be approximated by the parabolic potential. The small change in the resonance frequency can be calculated as equation (24). By measuring the polarity of the frequency shift, one can distinguish whether the interaction is attractive or repulsive from equation (24). Figure 7 shows an illustration of the relationship between frequency shift polarity and interaction

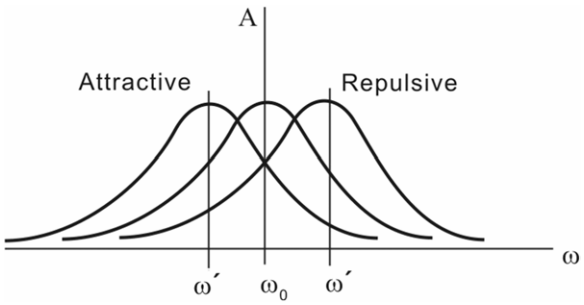

Figure 7. Illustration of the relationship between the frequency shift and interacting force direction. The x-axis is the angular frequency of the driving force and the y-axis is the amplitude of cantilever displacement. Attractive (repulsive) interacting force decreases (increases) the resonance frequency of the cantilever.

polarity. The x-axis is the angular frequency of the driving force and the y-axis is the amplitude of the cantilever displacement q.

From equation (24), one notices that this model is not the force, but the force gradient. One important point is that no uniform force ($\mathrm{d}F_{\mathrm{ts}}/\mathrm{d}z = 0$) causes frequency shifts in harmonic approximation. The uniform external force only changes the equilibrium point (D in figure 3(a)) of the harmonic oscillator, which is not measured in NC-AFM.

4.1.2. Minimum Detectable Force. Let us estimate the minimum detectable force gradient in harmonic approximation. To have the maximum sensitivity of amplitude, one would drive the cantilever with the frequency where the A versus ω curve has the steepest slope in figure 7. The angular frequency ω_{m} at the maximum slope is given by $\omega_{\mathrm{m}} \simeq \omega_0(1 \pm 1/\sqrt{8}Q)$ [43]. At this point, the slope is given by

$$\frac{\partial A}{\partial \omega} = \frac{4A_0 Q}{3\sqrt{3}\omega_0}. \tag{25}$$

For small force gradient $\mathrm{d}F_{\mathrm{ts}}/\mathrm{d}z$, $\Delta\omega = \omega_0(\mathrm{d}F_{\mathrm{ts}}/\mathrm{d}z)/2k$, and an amplitude change ΔA is given by

$$\Delta A = \frac{2A_0 Q}{3\sqrt{3}k}\frac{\mathrm{d}F_{\mathrm{ts}}}{\mathrm{d}z}. \tag{26}$$

The dominant noise source on AM-AFM at room temperature is the thermal fluctuation of the cantilever [43]. The thermal energy excites the cantilever on which vibration amplitude is $A_{\mathrm{T}} = \sqrt{2k_{\mathrm{B}}T/k}$. Its vibrational amplitude noise N is measured with a bandwidth B, at a frequency ω_{m}, $N = \sqrt{4k_{\mathrm{B}}TQB/k\omega_{\mathrm{m}}}$ [47]. At a given temperature, it is not possible to measure the amplitude smaller than the thermal vibration amplitude. Therefore, the minimum detectable force is determined by the thermal vibration. By equating N and ΔA in equation (26), the minimum detectable force gradient $(\mathrm{d}F_{\mathrm{ts}}/\mathrm{d}z)_{\mathrm{min}}$ is given as

$$\left(\frac{\mathrm{d}F_{\mathrm{ts}}}{\mathrm{d}z}\right)_{\mathrm{min}} = \frac{1}{A_0}\sqrt{\frac{27k k_{\mathrm{B}}TB}{Q\omega_0}}, \tag{27}$$

with an approximation $\omega_{\mathrm{m}} \simeq \omega_0$. From equation (27), it was found that the spring constant k must be small and the Q value and ω_0 must be high to increase the sensitivity of AM-AFM.

Even though the harmonic model described above is helpful for a conceptual understanding of the dynamic AFM principle, in most cases the harmonic model fails to provide quantitative agreement with the experimental data [4]. The failure of the harmonic model stems from three assumptions: (1) the tip–sample interaction does not transfer energy. (2) The force gradient is independent of the tip–sample distance. (3) The force gradient is much smaller than k. In most experiments, at least one of these assumptions has been shown to be invalid [4].

4.1.3. AM-AFM: damping effect. Anczykowski *et al* [51] suggested a model to relate the cantilever vibration amplitude and its damping effect. They assumed that the average energy $\overline{P}_{\mathrm{in}}$ supplied by the actuator is equal to the energy dissipation. The energy dissipation is a sum of the average power dissipated by the motion of the cantilever $\overline{P}_0$ and by tip–sample interaction $\overline{P}_{\mathrm{tip}}$;

$$\overline{P}_{\mathrm{in}} = \overline{P}_0 + \overline{P}_{\mathrm{tip}}. \tag{28}$$

The vibration of cantilever $q(t)$ is given by the motion of the external driver (Z-actuator) $z_{\mathrm{d}}(t)$. Typically, $|q(t)| \gg |z_{\mathrm{d}}(t)|$, because general cantilevers have a pretty high Q-value ($Q > 10^2$). $\overline{P}_{\mathrm{in}}$ can be simply calculated as

$$P_{\mathrm{in}} = F_{\mathrm{d}}(t)\dot{z}_{\mathrm{d}}(t) = k[q(t) - z_{\mathrm{d}}(t)]\dot{z}_{\mathrm{d}}(t). \tag{29}$$

Considering a sinusoidal driving force $z_{\mathrm{d}}(t) = A_{\mathrm{d}}\cos(\omega t)$, the deflection of the cantilever is also given by a sinusoidal solution with a phase: $q(t) = A\cos(\omega t - \phi)$. Now, one can calculate the average power driven by integrating equation (29) over one period:

$$\overline{P}_{\mathrm{in}} = \frac{1}{T}\int_0^T P_{\mathrm{in}}(t)\,\mathrm{d}t = \frac{1}{2}k\omega A_{\mathrm{d}}A\sin\phi. \tag{30}$$

On resonance, $\phi = 90^\circ$ and $\overline{P}_{\mathrm{in}}$ has the maximum power. Assuming a dissipative force $F_0 = b\dot{q}(t)$ with damping coefficient b, the average power dissipated by the motion of the cantilever $\overline{P}_0$ can be written as

$$\overline{P}_0 = \frac{1}{T}\int_0^T |b\dot{q}(t)\dot{q}(t)|\,\mathrm{d}t = \frac{1}{2}b\omega^2A^2. \tag{31}$$

The damping coefficient b is related to the experimental quantity Q-value as $b = k/(Q\omega_0)$. Combining equations (28), (30) and (31), the tip–sample interaction dissipation $\overline{P}_{\mathrm{tip}}$ is

$$\overline{P}_{\mathrm{tip}} = \overline{P}_{\mathrm{in}} - \overline{P}_0 = \frac{1}{2}\frac{k\omega}{Q}\left[QA_{\mathrm{d}}A\sin\phi - A^2\frac{\omega}{\omega_0}\right]. \tag{32}$$

Considering that the driving frequency ω is close to the cantilever resonance frequency ω_0 and the cantilever oscillation amplitude A_0 is amplified as $A_0 \simeq QA_{\mathrm{d}}$, the above equation is simplified as follows:

$$\overline{P}_{\mathrm{tip}} = \frac{1}{2}\frac{k\omega_0}{Q}[A_{\mathrm{d}}A\sin\phi - A^2]. \tag{33}$$

By using this equation, the power dissipation can be estimated from the amplitude and phase changes of the cantilever.

4.2. AM force spectroscopy

By measuring the amplitude change of the cantilever as it approaches a sample and retracts, one can get a force–distance curve, which is called AM-AFM spectroscopy. In terms of experimental accessibility, AM-AFM is more easily implemented than FM-AFM. But, in terms of theoretical analysis, FM-AFM is more straightforward as shown in harmonic approximation as equation (24). The FM-AFM is well formulated and the tip–sample interaction potential can be extracted from the theoretical formula, which is discussed in section 5 [5,48]. On the other hand, a theory for tapping-mode AM-AFM explaining the coexistence of two stable oscillations was reported by Paulo and Garcia [57] and a general theory for AM-AFM was developed by Lee and Jhe [50] who derived an integral equation for amplitude in AM-AFM.

4.2.1. Theory for AM-AFM. The Lee and Jhe formalism [50] starts with the harmonic oscillator model described by equation (16) in section 3. Considering the damping coefficient $b = k/(Q\omega_0)$;

$$m\ddot{q} + kq + b\dot{q} = F_{\rm ts} + F_0\cos(\omega t). \tag{34}$$

From the solution in equation (17), consider the steady term with offset which could be caused by a constant external force:

$$q(z,t) = q_0(z) + A(z)\sin[\omega t + \theta(z)], \tag{35}$$

where the amplitude $A(z)$ and the phase $\theta(z)$ are assumed to be functions of z.

In general, $F_{\rm ts}$ is a nonlinear function of the tip–sample distance z, which contains both conservative $F_{\rm c}(z)$ and dissipative (or non-conservative) $F_{\rm nc}$ forces.

$$F_{\rm ts} = F_{\rm c}(z) + F_{\rm nc}, \tag{36}$$

where $F_{\rm c}$ is assumed to depend only on the distance z. One can calculate the dissipation energy $E_{\rm dis}$ caused by $F_{\rm nc}$ by integrating the dissipation power over one period;

$$E_{\rm dis} = \int_0^T {\rm d}t\dot{q}F_{\rm nc}, \tag{37}$$

$$= \int_0^T {\rm d}t\dot{q}(m\ddot{q} + kq + b\dot{q} - F_{\rm c} - F_0\cos(\omega t)). \tag{38}$$

By inserting equation (35) into equation (38), a general dissipative energy equation is obtained;

$$E_{\rm dis} = -\pi(FA\cos\theta - b\omega A^2). \tag{39}$$

The same result on $E_{\rm dis}$ was obtained by Anczykowski *et al* [51] with a different approach, as shown in equation (33). The above equation is always valid as long as the cantilever motion is harmonic [50].

To analyze the cantilever motion in detail, we consider the non-conservative force $F_{\rm nc} = -\Gamma(z)\dot{z}$, where Γ indicates the effective damping coefficient of the dissipative interaction, which is a function of distance z. This non-conservative force includes the van der Waals, electrostatic, capillary meniscus forces. Equation (34) can be written as follows:

$$m\ddot{q} + b\dot{q} + kq = F_{\rm c}(z+q) + F_0\cos(\omega t) - \Gamma(z+q)\dot{q}, \tag{40}$$

where the tip–sample distance in right terms is given by the instantaneous distance $z+q$, as shown in figure 3(*b*). In AM-AFM experiments, z is controlled by the Z-actuator through the feedback signal proportional to the instant change of the amplitude q. Inserting equation (35) into equation (40), multiplying both sides by $\sin(\omega t+\phi)$ and $\cos(\omega t+\phi)$ and integrating over a period with an approximation $|q_0| \ll |z + A\sin(\omega t+\theta)|$, two master equations are obtained as

$$\int_0^\pi \frac{{\rm d}\tau}{\pi} F_{\rm c}(z + A\cos(\tau))\cos(\tau) = -\frac{F}{2}\sin(\theta) + \frac{A}{2}(k - m\omega^2), \tag{41}$$

$$\int_0^\pi \frac{d\tau}{\pi}\Gamma(z + A\cos(\tau))\sin^2(\tau) = \frac{1}{2}\left(\frac{F}{A\omega}\cos(\theta) - b\right), \tag{42}$$

where the amplitude $A = A(z)$ and the integration over τ is independent of z. From the master equations given by equations (41) and (42), the amplitude and phase are estimated numerically if $F_{\rm c}$ and Γ are known. Moreover, if the amplitude and phase are measured experimentally, the interacting forces $F_{\rm c}$ and Γ can be determined by using these master equations. The integration form of the master equations can be inverted as analytically accessible forms using Laplace transform of certain functions $C(\lambda)$ and $\gamma(\lambda)$, respectively, as [48–50]

$$F_{\rm c}(z) \equiv \int_0^\infty {\rm d}\lambda {\rm e}^{-\lambda z}C(\lambda), \tag{43}$$

$$\Gamma(z) \equiv \int_0^\infty {\rm d}\lambda {\rm e}^{-\lambda z}\gamma(\lambda). \tag{44}$$

Inserting equations (43) and (44) into equations (41) and (42), the equations are changed as

$$\int_0^\infty {\rm d}\lambda C(\lambda){\rm e}^{-\lambda z}I_1(\lambda A) = \frac{F}{2}\sin(\theta) - \frac{A}{2}(k - m\omega^2), \tag{45}$$

$$\int_0^\infty {\rm d}\lambda\gamma(\lambda){\rm e}^{-\lambda z}\frac{I_1(\lambda A)}{\lambda A} = \frac{1}{2}\left(\frac{F}{A\omega}\cos(\theta) - b\right), \tag{46}$$

where $I_1(\lambda A)$ is the modified Bessel function of the first kind of order one, specifically

$$I_1(\lambda A) = \sum_{k=0}^{\infty}\frac{(\lambda A)^{2k+1}}{2^{2k+1}k!(k+1)!}. \tag{47}$$

With this Bessel function, the integral equations (45) and (46) are changed into

$$\sum_{k=0}^{\infty}\frac{(\lambda A)^{2k+1}}{2^{2k+1}k!(k+1)!}\frac{{\rm d}^{2k+1}}{{\rm d}z^{2k+1}}F_{\rm c}(z) = -\frac{F}{2}\sin(\theta) + \frac{A}{2}(k - m\omega^2), \tag{48}$$

$$\sum_{k=0}^{\infty}\frac{A^{2k}}{2^{2k+1}k!(k+1)!}\frac{{\rm d}^{2k}}{{\rm d}z^{2k}}\Gamma(z) = \frac{1}{2}\left(\frac{F}{A\omega}\cos(\theta) - b\right), \tag{49}$$

with the boundary conditions

$$\frac{{\rm d}^k}{{\rm d}z^k}F_{\rm c}(z) = \frac{{\rm d}^k}{{\rm d}z^k}\Gamma(z) = 0 \qquad \text{as } z\to\infty,$$
$$k = 0, 1, 2, \ldots . \tag{50}$$

By numerical calculation of equations (48) and (49), the exact solution of the tip–sample interaction can be determined from the measurable amplitude and phase. Because the higher order terms contribute less significantly, one can consider the first few order terms $k = 0$, 1 and 2. For example, consider the first order term $k = 0$ only. Then, one can obtain the following equations:

$$F_c^{(1)}(z) = \int_z^\infty \mathrm{d}z \left[\frac{F}{A}\sin\theta - (k - m\omega^2)\right] \tag{51}$$

$$\Gamma^{(1)}(z) = \frac{F}{A\omega}\cos\theta - b. \tag{52}$$

Notice that A and θ are functions of z in the above equations. The force gradient of the tip–sample interacting force can be obtained by differentiating equation (51), which is equivalent to the elasticity of the sample or water meniscus adsorbed on the sample [50]. The energy dissipation

$$E_{\mathrm{dis}} = \int_{\mathrm{period}} (-\Gamma^{(1)}\dot{z})\,\mathrm{d}z \tag{53}$$

can be calculated from equation (52). In conventional AM-AFM, the amplitude A is kept constant by a feedback control, the simultaneously acquired phase θ provides the information on energy dissipation.

4.2.2. Nonlinear behavior in amplitude versus distance curves. Aime *et al* [52] reported a nonlinear dynamic behavior of the cantilever using the variational method and the least action law. They pointed out that for an oscillator set at a driving frequency slightly below the resonance one, a bifurcation from a monostable to a bistable state may occur [53]. In their theoretical analysis, the variational method was used, which is based on the principle of the least action law [52]. The action $S[x(t)]$ is a functional of the path $x(t)$ and is extremal between two fixed instants.

$$S[x(t)] = \int_{t_a}^{t_b} L(x, \dot{x}, t)\,\mathrm{d}t, \tag{54}$$

where L is the Lagrangian of the system. They considered only harmonic solutions $q(t) = A(z)\cos[\omega t - \phi(z)]$ as Lee and Jhe's formalism does [50]. The Lagrangian is obtained from a sphere tip and plane sample interaction [18],

$$L = T - U + W, \tag{55}$$

$$= \frac{1}{2}m\dot{q}^2 - \left[\frac{1}{2}kq^2 - qF_0\cos(\omega t) - \frac{A_{\mathrm{H}}R}{6(z-q)}\right] - bq\dot{q}, \tag{56}$$

where A_{H} is the Hamaker constant, R the radius of the tip and b the damping coefficient. In equation (56), the first term is the kinetic energy of the cantilever, the second is the potential energy of the cantilever, the third is the average driving energy given by the Z-actuator, the fourth is the van der Waals interaction of the sphere-plane model and the final term is the dissipation energy of the cantilever. The action S has two parameters A and ϕ. The variational principle gives two differential equations:

$$\frac{\partial S}{\partial A} = 0, \tag{57}$$

$$\frac{\partial S}{\partial \phi} = 0. \tag{58}$$

From the above equations, two coupled equations were obtained;

$$\cos\phi = Qa(1 - u^2) - \frac{\alpha}{3}\frac{a}{(d^2 - a^2)^{3/2}}, \tag{59}$$

$$\sin\phi = au, \tag{60}$$

where $a = A/A_0$, $d = z/A_0$, $u = \omega/\omega_0$, Q is the quality factor and the dimensionless parameter $\alpha = HRQ/(kA_0^3)$. By solving equations (59) and (60), the relation between the amplitude and the distance is obtained;

$$d_\pm = \sqrt{a^2 + \left(\frac{\alpha}{3[Q(1-u^2) \pm \sqrt{1/a^2 - u^2}]}\right)^{2/3}}. \tag{61}$$

From the above equation, u can be obtained in closed form;

$$u = \left(\frac{1}{a^2} - \left[\frac{1}{2Q}\left(1 \pm \sqrt{1 - 4Q^2\left(\frac{1}{a^2} - \frac{\alpha}{3Q(d^2-a^2)^{3/2}}\right)}\right)\right]^2\right)^{1/2}. \tag{62}$$

Because A is kept constant close to A_0 for AM-AFM measurement in general, the resonance frequency shift is obtained assuming $a \simeq 1$;

$$\frac{\Delta f}{f_0} = 1 - u = 1 - \sqrt{1 - \left(\frac{1 + \sqrt{1 + 4Q\alpha/3(d^2-1)^{3/2}}}{2Q}\right)^2}. \tag{63}$$

From equation (62), the cantilever frequency spectra can be obtained because the tip is close to the sample. For instance, when a high Q-valued cantilever ($Q = 2 \times 10^4$) is close to the sample, but not touching it ($z = 1.02A_0$), the spectrum changes with different spring constants. ($k = 1$, 10 and 100 N m^{-1}) are shown in figure 8, where $A_{\mathrm{H}}R = 10^{-27}$ J m. While for the stiff cantilever ($k = 100$) spectrum distortion is not significant, for a soft cantilever with $k = 1$ there is a significant distortion of the spectrum. For example, if one chooses the excitation frequency $f \leqslant f_0$, there are two possible amplitudes (high and low states) which can be interpreted as a bifurcation starting point of chaotic phenomenon [52]. Figure 9 shows the spectra with different tip-sample distances ($d = z/A_0 = 1.01$, 1.05 and 2.00), where $Q = 2 \times 10^4$, $A_{\mathrm{H}}R = 10^{-27}$ J m and $k = 10$ N m^{-1}. Similarly to the behavior for the soft spring constants, the close tip–sample distance results in the bistable state.

Experimentally and theoretically, this bistable state was reported in several works [4, 54–57]. Moreover, in some specific conditions such as small tip–sample distance and large

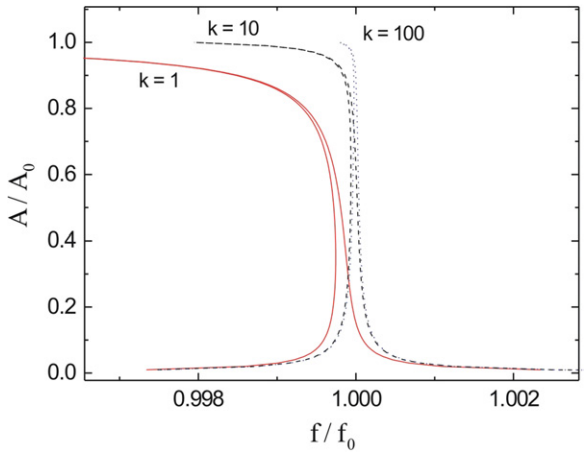

Figure 8. Cantilever frequency spectra calculated from equation (62). When a high Q-valued cantilever ($Q = 2 \times 10^4$) is close to the sample ($z = 1.02A_0$), the spectra with different spring constants ($k = 1$, 10 and 100 N m^{-1}) are shown, where $A_H R = 10^{-27}$ J m. For a soft cantilever $k = 1$, the original Lorentzian spectrum is distorted significantly.

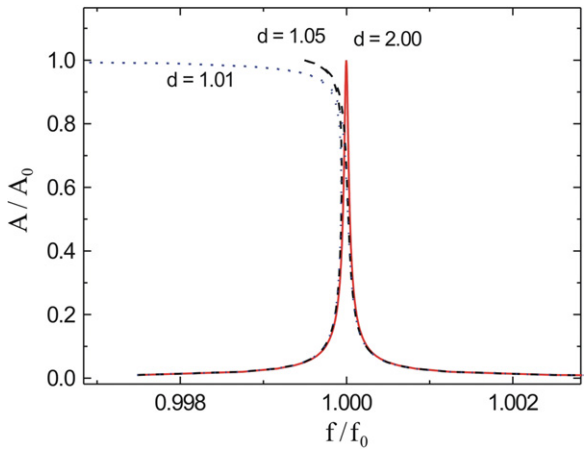

Figure 9. The spectra with different tip-sample distances ($d = z/A_0 = 1.01$, 1.05 and 2.00) under the condition of $Q = 2 \times 10^4$, $A_H R = 10^{-27}$ J m and $k = 10$ N m^{-1}.

amplitude, more than two or chaotic solutions were obtained [58, 59].

Moreover, Lee and Jhe formalism results in similar bistable behavior with hysteresis [50]. The hysteresis in the force–distance curve was found by numerical calculation to demonstrate the validity of formalism. The Lennard–Jones-type force was adapted consisting of z^{-6} repulsive and $-z^{-2}$ attractive terms [48, 47].

$$F_{\text{int}} = F_0 \left(\frac{l^4}{3z^6} - \frac{1}{z^2} \right), \tag{64}$$

where F_0 is a constant representing force strength and l is the characteristic length representing force range. Inserting equation (64) into equations (41) and (42) and solving them numerically, the amplitude and phase curves were obtained as shown in figure 10. Figures 10(a), (c) and (e) show the amplitude changes, while (b), (d) and (f) show the phase changes for different free amplitudes A_0 with $F_0 Q/(l^3 k) = 5$. In figure 10(a), (c) and (e), the x and y-axes represent the normalized tip–sample distance z/l and amplitude A/l, respectively. In particular, for regions (surrounded by A–B–C–D) of z/l, there are three solutions of A/l, consisting of two stable ($\overline{\text{AB}}$, $\overline{\text{CD}}$) and one unstable ($\overline{\text{BD}}$) states. For instance, figure 10(a) displays the amplitude behavior for the amplitude–distance curve. When the tip approaches the sample, increasing attractive force causes a decrease of the amplitude A. Through point A in figure 10(a), the amplitude follows the lower branch before point B. At the point B, the amplitude jumps to the upper stable point C, and follows the trace to the left. It is noticeable that as the tip is close to the sample ($z/l < 1$), the amplitude A becomes almost zero. In the retracting process, the amplitude follows the upper trace (C $\rightarrow$ D $\rightarrow$ A), producing hysteresis behavior. However, hysteresis does not occur for the small amplitude cantilever, as shown in figure 10(e), where $A_0/l = 0.1$. Therefore, the bistable or hysteresis behavior in the large amplitude case may be related to the cantilever motion vibrating between the jump-to-contact and jump-off-contact points as described in static AFM. In this case, very sensitive behavior for A and the phase are shown at $z/l \simeq 1$. The phase change shows a dramatic transition from hysteresis behavior to monotonic dependence at $z/l \simeq 1$ as shown in figure 10(b), (d) and (f). Especially, one can get very sensitive and linear feedback control by using the phase signal under the condition of $A_0/l \leqslant 0.1$ in the repulsive region. This is shown in figure 10(f).

Lee and Jhe also demonstrated the accuracy of their formalism by reconstructing the tip–sample interaction forces from the approach curves shown in figure 10. They chose the data of A and phase from $z = \infty$ to $z = 0$ following the path $\infty \rightarrow$ A $\rightarrow$ B $\rightarrow$ C $\rightarrow 0$ and numerically calculated the F_c using equation (48) up to 3rd order ($k = 0$, 1 and 2). The resulting forces (dotted lines) are shown in figure 11(a)–(c) with the assumed force (solid line) in equation (64). Figures 11(a)–(c) correspond to $A_0/l = 1$, 0.8 and 0.1, respectively. The first order solution is obtained from equation (51) and the second and third order solutions are given by numerical integration in equation (48). As shown in figures 11(a)–(c), the reconstructed forces up to the higher order term show better agreement with the original Lennard–Jones force. Especially, in the case of small amplitude $A_0/l = 0.1$, only first order approximation solution is good enough to reconstruct the original force.

In order to figure out the tendency of the accuracy as a function of λA in equation (47), the polynomials P_1, P_2, P_3 and I_1 are depicted in figure 11(d), where P_n is the sum of the terms from $k = 0$ to $k = n-1$ in the right hand of equation (47). As shown in figure 11(d), in the case of small amplitude $\lambda A < 1$, P_1 and I_1 are very close, while the difference between P_1 and I_1 grows as λA increases. Therefore, to obtain an accurate estimation for large amplitude, inclusion of higher order polynomial terms is required.

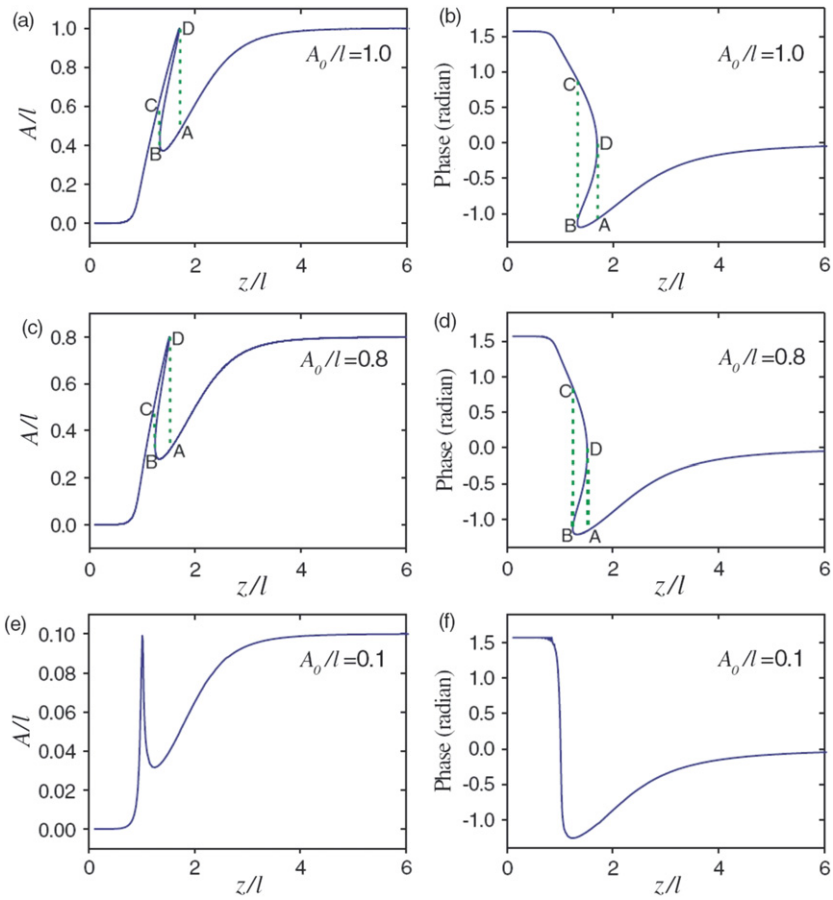

Figure 10. For the Lennard–Jones-type force, the amplitude and phase curves were calculated numerically. (*a*), (*c*) and (*e*) show the amplitude changes and (*b*), (*d*) and (*f*) show the phase changes for different free amplitudes A_0, with $F_0Q/(l^3k) = 5$. Reprinted figure with permission from [50]. (http://link.aps.org/abstract/PRL/v97/p036104) Copyright (2006) by the American Physical Society.

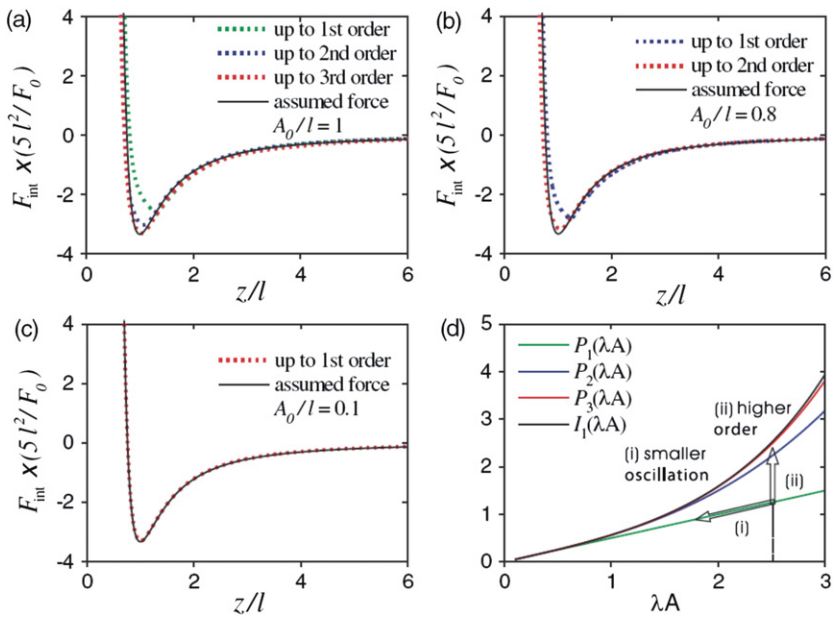

Figure 11. (*a*)–(*c*) Numerical calculations of the F_c using equation (48) up to 3rd order ($k = 0$, 1 and 2). From the data of A and phase from $z = \infty$ to $z = 0$ ($\infty \rightarrow A \rightarrow B \rightarrow C \rightarrow 0$), forces (· · · · · ·) are calculated. The assumed force (——) in equation (64) is shown together. (*a*)–(*c*) correspond to $A_0/l = 1$, 0.8 and 0.1, respectively. (*d*) shows the polynomials P_1, P_2, P_3 and I_1. While for small amplitude $\lambda A < 1$ P_1 and I_1 are very close, the difference between P_1 and I_1 grows as λA increases. Reprinted figure with permission from [50]. Copyright (2006) by the American Physical Society.

5. FM atomic force microscopy and spectroscopy

5.1. FM atomic force microscopy

The time constant ($1/\alpha = 2Q/\omega_0$) of the amplitude as shown in equation (17) is excessively long for a vacuum and low-temperature environment. These conditions are essential for a high sensitivity measurement. This is a critical disadvantage for AM-AFM. The inverse of the time constant determines the bandwidth of the AFM operation. Typically, in vacuum, the quality factor Q is increased up to $\sim 10^5$ and the resulting bandwidth will be lower than ~ 1 Hz. This means the 256×256 pixel imaging will take roughly one day. In order to overcome the long time constant problem, the frequency modulation (FM) mode AFM was developed. The response time of the frequency change is as short as a single oscillation period [5].

In order to provide fast scanning ability with a high Q-valued cantilever, the FM-AFM was developed by Albrecht *et al* [60]. Figure 12 shows the original diagram of the FM detection electronic circuit. The circuit consists of two main parts: active oscillator and FM demodulator as indicated in dashed boxes in figure 12. The active oscillator excites the cantilever to vibrate it with its resonance frequency, by using positive feedback of the oscillation. The cantilever is mounted on a vibrator such as a bimorph. The vibrator is excited by an electric ac-voltage and its mechanical motion is transmitted to the cantilever vibration. If the frequency of the excitation voltage is close to the cantilever resonance frequency, the mechanical motion of the cantilever is amplified, which is detected by a quadrature photo diode or the phase sensitive photo diode (PSPD). The amplitude of the PSPD ac-signal is held constant by an automatic gain controller (AGC). To suppress noise, a bandpass filter passing signals with frequency range near the resonance frequency is added. After the phase is adjusted through a phase shifter, the resulting signal is fed into the bimorph. With proper phase control, the cantilever is oscillated due to the positive feedback. This active oscillator is supposed to oscillate the cantilever with its resonance frequency and constant amplitude.

The FM demodulator depicted in the lower box in figure 12 detects the frequency change of cantilever resonance frequency. By the limiter the amplitude of the PSPD signal is limited to a certain value, and the phase detector measures the phase difference between the limiter and LC resonator outputs. The phase detector generates dc voltages proportional to the frequency of the cantilever. The threshold detector is used to provide a pullback signal to protect the cantilever or tip when the PSPD outputs abnormal signals with low amplitude. The resulting frequency shift signal is fed into a high voltage (HV) amplifier to provide the feedback signal to the Z-directional piezo scanner.

Recently, instead of using the FM demodulator, a phase-locked loop (PLL) has been employed for FM-AFM [17, 61, 62]. As shown in figure 13, the PLL consists of a voltage controlled oscillator (VCO) and a phase detector. The VCO generates a reference signal (V_{out}) in which frequency is controlled by input voltage. V_{out} is fed into the actuator to excite the cantilever and the phase change of the PSPD signal is compared with the phase of V_{out} by the phase detector. The phase change is caused by the frequency change affected by the tip–sample interaction. The phase signal is fed into VCO input as a feedback signal after the high frequency noise is filtered out by a low pass filter. Atia and Davis [61] used an active oscillator circuit to vibrate the cantilever and an external reference signal was applied to measure the phase shift of the cantilever, rather than using the VCO.

5.1.1. Stability. As discussed in section 3, the soft cantilever jump-to-contact in the attractive force region. For non-contact AFM, the cantilever should not jump-to-contact. This condition is [5]

$$k > \max\left(-\frac{\partial^2 V_{\text{ts}}}{\partial z^2}\right) = k_{\text{ts}}^{\max}, \tag{65}$$

where k_{ts} is the interacting force gradient. On the other hand, even for soft cantilevers, jump-to-contact instability can be avoided by increasing vibration amplitude [21]:

$$kA > \max(-F_{\text{ts}}) = F_{\text{ts}}^{\max}. \tag{66}$$

5.1.2. Theories for FM-AFM. As discussed in the previous section, harmonic approximation provides an intuitive understanding of the relationship between frequency shift and tip–sample interaction described in equation (24). The first order approximation of equation (24) is given by

$$\Delta f \simeq -f_0 \frac{k_{\text{ts}}}{2k}, \tag{67}$$

where the force gradient $k_{\text{ts}} = \partial F_{\text{ts}}/\partial z$. Harmonic approximation is only applicable for a small amplitude vibrating cantilever because it is based on the assumption that the distance dependence of the force is linear in the range of the cantilever motion. However, general commercial AFM has an amplitude larger than 100 nm, which is much larger than force range such as van der Waals force, short-range electrostatic force or chemical force. Thus, harmonic approximation can be applied for long range forces only (i.e. magnetic force microscopy) rather than short-range forces.

Giessibl suggested the relationship between frequency shift and interacting force by using a Hamilton–Jacobi method, firstly [21]

$$\Delta f = -\frac{f_0}{kA^2}\langle F_{\text{ts}} q \rangle, \tag{68}$$

where $\langle \ldots \rangle$ means the average of the argument over a period. The same result was derived by other methods such as in the canonical perturbation-theory [63–67], and Fourier series method [66, 68].

Among them, the Fourier series method will be discussed to derive equation (68). This method starts from the simplified equation of motion ignoring the damping and driving force terms in equation (34):

$$m\ddot{q} = -kq + F_{\text{ts}}. \tag{69}$$

The cantilever motion is assumed to be harmonic and its Fourier series is given by

$$q(t) = \sum_{n=0}^{\infty} a_n \cos(n\omega t). \tag{70}$$

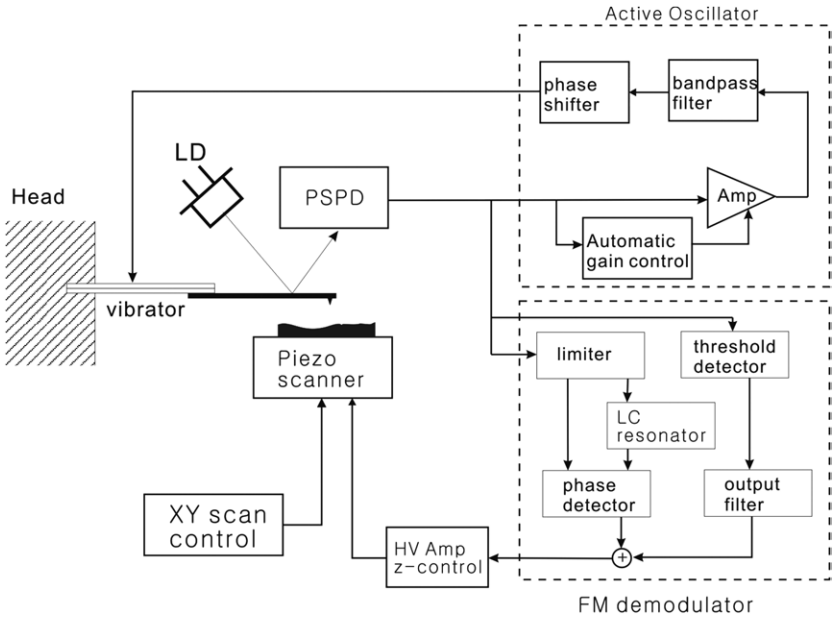

Figure 12. Schematic design of the FM-AFM detection electronics. The circuit consists of two main parts: active oscillator and FM demodulator as indicated in the boxes. The active oscillator excites the cantilever with resonance frequency by using positive feedback from the oscillation.

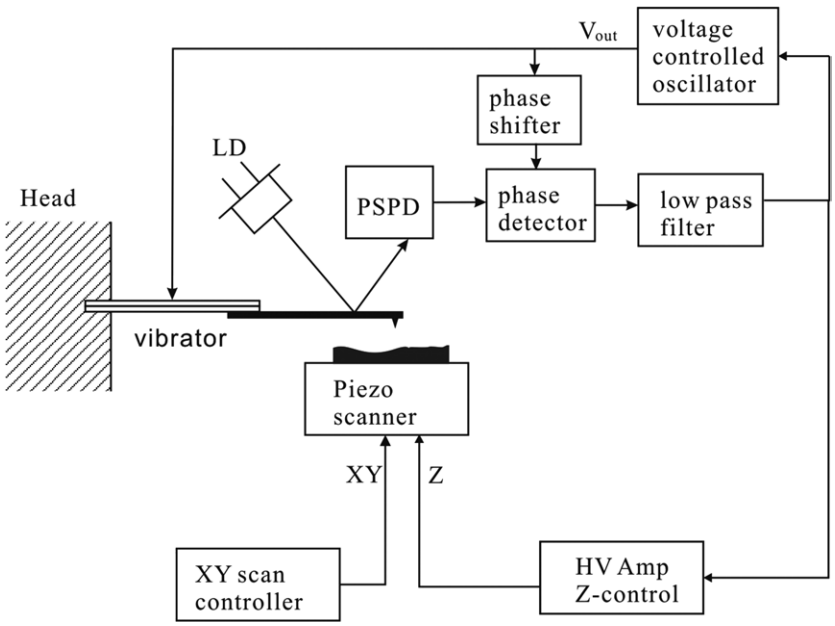

Figure 13. Schematics of a PLL based FM-AFM setup. The PLL consists of a VCO and a phase detector. The VCO generates a reference signal (V_{out}) of which frequency is controlled by its input voltage. V_{out} is fed into the vibrator and the phase change of the PSPD signal is compared with the phase of V_{out} by the phase detector.

By inserting equation (70) into equation (69), the Fourier components are determined:

$$\sum_{n=0}^{\infty} a_n[-(n\omega)^2)m + k]\cos(n\omega t) = F_{ts}(z+q). \tag{71}$$

By multiplying by $\cos(n'\omega t)$ and integrating over a period, and replacing n' by n, a_n is given as

$$a_n[-(n\omega)^2)m + k]\pi(1+\delta_{n0}) = \omega\int_0^T F_{ts}(z+q)\cos(n\omega t)\,\mathrm{d}t. \tag{72}$$

Ignoring the higher order terms, the cantilever motion can be approximated as $q(t) \simeq A\cos(\omega t)$, which corresponds to the case of $n = 1$. The frequency can be written as $f = f_0 + \Delta f = \omega/(2\pi)$, where $f_0 = (1/2\pi)\sqrt{k/m}$. Assuming that $|\Delta f| \ll f_0$, the first order term is given by

$$\Delta f = -\frac{f_0}{kA}\int_0^T F_{ts}(z+q)\cos(\omega_0 t)\,\mathrm{d}t \tag{73}$$

$$= -\frac{f_0}{kA^2}\langle F_{ts}(z+q)q\rangle. \tag{74}$$

Table 1. γ_{1A} and $\sqrt{V_{ts}F_{ts}}$ for three different types of tip–sample interacting forces. $\Gamma(n)$ represents the Gamma function. Adapted from [4].

Type	$F_{ts}(z)$	γ_{1A}	$\sqrt{\lvert V_{ts}F_{ts}\rvert}$
Inverse power	$\frac{C}{z^n}$	$\frac{1}{\sqrt{2\pi}}\frac{\Gamma(n-1/2)}{\Gamma(n)}\frac{C}{d^{n-1/2}}$	$\frac{1}{\sqrt{n-1}}\frac{C}{d^{n-1/2}}$
Power	$C(-z)^m$	$\frac{1}{\sqrt{2\pi}}\frac{\Gamma(m+1)}{\Gamma(m+3/2)}C(-d)^{m+1/2}$	$\frac{C}{\sqrt{m+1}}C(-d)^{m+1/2}$
Exponential	$F_0e^{-\kappa z}$	$\frac{1}{\sqrt{2\pi\kappa}}F_0e^{-\kappa d}$	$\frac{1}{\sqrt{\kappa}}F_0e^{-\kappa d}$

The above equation is a central equation for FM-AFM analysis, which provides good approximation especially for large amplitude measurement.

5.1.3. Small amplitudes. In many cases, tip–sample interacting force can be described by an inverse power law (e.g. van der Waals interaction):

$$F_{ts} = -\frac{C}{z^n}. \tag{75}$$

By inserting equation (75) into equation (74), the frequency shift is given by

$$\Delta f = \frac{1}{2\pi}\frac{f_0}{kA_0}\frac{C}{d^n}\int_0^{2\pi}\frac{\cos x}{[1+(A_0/d)(\cos x+1)]^n}\,dx, \tag{76}$$

where $d = z - A_0$ is the minimum distance between the sample and the tip as depicted in figure 3(*b*). Because of $A_0 \ll d$, the above equation can be approximated with the Taylor expansion for the integration function. Therefore,

$$\Delta f \simeq -n\frac{f_0}{2k}\frac{C}{d^{n+1}} = \frac{f_0}{2k}\frac{\partial^2 V_{ts}}{\partial z^2}\Big|_{z=d}. \tag{77}$$

This result is identical to the result for harmonic approximation, equation (67) [21].

5.1.4. Large amplitudes. In the case of a large amplitude cantilever ($A_0 \gg d$), most tip–sample interaction occurs at a minimum distance between the tip and the sample (at $x \simeq \pi$ in equation (76)) and $\cos x$ can be approximated as $-1+(x-\pi)^2$ in the vicinity of $x = \pi$. Ignoring 1 in the denominator in equation (76)), the frequency shift is given as

$$\Delta f \simeq -\frac{1}{\sqrt{2}\pi}\frac{f_0}{kA_0^{3/2}}\frac{C}{d^{n-1/2}}\int_{-\infty}^{\infty}\frac{1}{(1+y^2)^n}\,dy, \tag{78}$$

where $y = \sqrt{A_0/2d}(x-\pi)$. In the above equation, all the terms except $f_0/(kA_0^{3/2})$ are not strongly dependent on k, A_0 and f_0. For all inverse power law and exponential decaying forces, Δf is proportional to $f_0/(kA_0^{3/2})$. Therefore, a *normalized frequency shift* can be defined as

$$\gamma(d) \equiv \frac{kA_0^{3/2}\Delta f}{f_0}. \tag{79}$$

$\gamma(d)$ is not dependent on the external parameters such as the amplitude, spring constant and resonance frequency of the cantilever. It represents the intrinsic contribution of the tip–sample interaction. From equation (74), one can get the normalized frequency shift

$$\gamma(d) = \frac{1}{\sqrt{2}\pi}\int_0^{2A_0}\frac{F_{ts}(d+z')}{\sqrt{z'}}\frac{1-z'/A_0}{\sqrt{1-z'/2A_0}}\,dz', \tag{80}$$

where $z' \equiv A_0[1+\cos(\omega_0 t)]$. In this expression $\gamma(d)$ still depends on A_0. However, for the large amplitude limit, $A_0 \to \infty$, the second factor in the integration can be approximated as unity [69] and an additional approximate form for the normalized frequency shift γ_{1A} is given by

$$\gamma_{1A} = \frac{1}{\sqrt{2}\pi}\int_0^{\infty}\frac{F_{ts}(d+z')}{\sqrt{z'}}\,dz'. \tag{81}$$

Even though γ_{1A} is given in simple form, it provides a good approximation especially for a large amplitude cantilever AFM. For various types of tip–sample forces, γ_{1A} was calculated as shown in table 1 [69]. While the inverse power law dependence in table 1 corresponds to an attractive force (e.g. van der Waals potential, electrostatic and magnetic forces) in the range $d > 0$, the power law forces describe repulsive force in the range $d < 0$. This includes Hertzian contact forces with $m = 3/2$ for a spherical tip on a flat surface and adhesion forces with $m = 0$ [3, 18].

On the other hand, Ke *et al* [70] performed a numerical calculation for Si surface with a Si tip, by using the Lennard–Jones potential and the Morse potential. Their approach is based on the energy conservation law for an oscillating cantilever with a large amplitude. They found that the frequency shift Δf for a large amplitude is proportional to $\sqrt{|V_{ts}F_{ts}|}$ in the non-contact region. For small amplitudes, Δf is proportional to F_{ts}. A similar result was reported by Giessibl and Bielefeld [69] for a large amplitude AFM. Ke *et al* defined a force range or decay length $\lambda = V_{ts}/F_{ts}$. For instance, in the case of exponential decaying force $F_{ts} = F_0\exp(-\kappa q)$, the force range is given by $\lambda = 1/\kappa$. In their approximation, the frequency shift is given by $\gamma_{1A} \simeq F_{ts}\sqrt{\lambda}$. In table 1, the force ranges are shown for different types of forces. $\sqrt{|V_{ts}F_{ts}|}$ is the same as $\sqrt{2\pi}\gamma_{1A}$.

5.2. FM force spectroscopy

By using FM-AFM, not only the topographic imaging, but also the force between the tip and the sample can be measured as a function of distance. After Lantz *et al*'s [75] remarkable research on the site dependent chemical force analysis using

FM-AFM, FM force spectroscopy has been used for the study of an atomic structure even with sub-atomic spatial resolution [76]. Hölscher *et al* [77] studied the measurement of conservative and dissipative tip–sample interaction forces with the FM-AFM. They found that the frequency shift is determined by the mean tip–sample force whereas the gain factor of the self-driven oscillator is related to dissipative or viscous interaction.

5.2.1. Separation of interactions. Experimentally, the measured frequency shift may include more than two different interactions, and the forces can be separated by frequency shift-distance measurement using FM-AFM. The total force is the vector sum of different forces, e.g. $F_{\rm tot} = F_{\rm el} + F_{\rm vdW} + F_{\rm chem}$, where $F_{\rm el}$ is the electrostatic force $F_{\rm vdW}$ is the van der Waals force and $F_{\rm chem}$ is the chemical force. The total force can be written as

$$F_{\rm tot} = -\pi\epsilon_0 U^2 \frac{R}{z} - \frac{A_H}{6}\frac{R}{z^2} - 2\kappa E_{\rm bond} {\rm e}^{-\kappa(z-\sigma)}, \qquad (82)$$

where U is the voltage difference between the tip and the sample. In the last Morse potential term, the repulsive component was not included, assuming that the tip does not touch the sample in the non-contact AFM. By using table 1, one can calculate the normalized frequency shift γ_{1A}, as a summation of each contribution:

$$\gamma_{1A} = -\pi\epsilon_0 U^2 \frac{R}{(\sqrt{2}z)^{1/2}} - \frac{A_{\rm H} R}{12\sqrt{2}z^{3/2}} - \frac{\sqrt{2}E_{\rm bond}}{\sqrt{\pi\kappa}} {\rm e}^{-\kappa(z-\sigma)}. \qquad (83)$$

Using the above equation, one can separate forces from the mixed frequency–distance curve. In log–log plot for the frequency–distance curve, the electrostatic force yields -0.5 slope and the vdW yields -1.5. Guggisberg *et al* [71] reported the separation of interactions from the frequency–distance curve measured by FM-AFM in UHV condition. From their frequency–distance curve, long-range electrostatic interaction was eliminated by applying null potential voltage U between the probing tip and the sample. The long-range vdW contribution was determined by fitting the data for distances ranging from 1 to 6 nm. After the vdW contribution was subtracted from the interaction curves, the remaining part corresponded to the short-range chemical interaction. The chemical interaction was found to decrease exponentially, which fitted the Morse potential. As a result, the chemical force between single atoms was measured by FM-AFM.

5.2.2. Fourier expansion and variational approach. In equation (72), all Fourier coefficients a_n with $n \neq 1$ are small compared with the amplitude of the harmonic term a_1. Here, the tip–sample interaction is weak. In the integrand of equation (72) $z + q = z + \sum_{k=0}^{\infty} a_k \cos(k\omega t)$ can be approximated as $d + a_1(1+\cos\omega t)$ (refer to figure 3(*b*)). Then,

$$a_n = \frac{1}{\pi(1+\delta_{n,0})} \frac{\omega_0^2}{k(\omega_0^2 - n^2\omega^2)} \times \int_0^T F_{\rm ts}[d + a_1(1+\cos\omega t)]\cos(n\omega t)\omega\,{\rm d}t. \qquad (84)$$

For $n = 0$, the Fourier components a_0 corresponds to the average deflection of the cantilever in its equilibrium position, as shown in static AFM ($\delta_{\rm c}$ in figure 3(*a*)):

$$a_0 = \frac{1}{2\pi k}\int_0^T F_{\rm ts}[d + a_1(1+\cos\omega t)]\omega\,{\rm d}t, = \frac{1}{2\pi k}\int_0^{2\pi} F_{\rm ts}[d + a_1(1+\cos\phi)]\,{\rm d}\phi. \qquad (85)$$

Typically, for a stiff cantilever used in non-contact AFM, k is larger than $10\,{\rm N\,m^{-1}}$ and a_0 has an insignificant value $\leqslant 0.01$ Å [4]. For $n = 1$, one can get the same result as equation (74) by using that $a_1 = A$ and

$$\frac{\omega_0^2 - \omega^2}{\omega_0^2} \simeq -2\frac{\Delta\omega}{\omega_0} = -2\frac{\Delta f}{f_0}. \qquad (86)$$

For anharmonic terms ($n > 1$), a_n can be obtained by changing variable with $u = \cos(\omega t)$ in the integration:

$$a_n = \frac{1}{2\pi}\frac{2\omega_0^2}{k(\omega_0^2 - n^2\omega^2)}\int_{-1}^{1} F_{\rm ts}[d + a_1(1+u)]\frac{T_n(u)}{\sqrt{1-u^2}}\,{\rm d}u, \qquad (87)$$

where $T_n(u) = \cos(n\cos^{-1}(u))$ is the nth Chebyshev polynomial of the first kind [4, 67]. Specifically, the polynomials are $T_0 = 1$, $T_1 = u$, $T_2 = 2u^2 - 1$ and $T_3 = 4u^3 - 3u$, and its recursion relation is given by $T_{n+1} = 2uT_n - T_{n-1}$. For $n = 1$ in equation (87), one can obtain the frequency shift

$$\Delta f(d) = \frac{f_0}{\pi k a_1}\int_{-1}^{1} F_{\rm ts}[d + a_1(1+u)]\frac{u}{\sqrt{1-u^2}}\,{\rm d}u. \qquad (88)$$

It is noticeable that the term $(1-u^2)^{-1/2}$ weights the tip–sample interacting force in the integration over a period. This kernel has two singularities at the turning points ($u = \cos\pi = \pm 1$). This can be explained by the fact that the velocity of the cantilever slows at the turning points. Therefore, the large amplitude sinusoidal motion of the cantilever can be sensitive to the interacting force which is exerted only at the lowest point ($u = -1$) of the motion.

5.2.3. Inversion procedure. From equation (88), the effective force gradient can be defined as $k_{\rm ts}^{\rm eff} = 2k\Delta f/f_0$, which can be written as

$$k_{\rm ts}^{\rm eff}(d) = \frac{2}{\pi A^2}\int_d^{d+2A} F_{\rm ts}(s) K_1\left(\frac{s-d}{A} - 1\right){\rm d}s \equiv \boldsymbol{A}(F_{\rm ts}), \qquad (89)$$

by changing variable $s = d + a_1(1+u)$, where $K_1 = u/\sqrt{1-u^2}$, $A = a_1$ and $\boldsymbol{A}$ is an operator defined in this equation. a_1 can be written as amplitude A, because a_1 is the Fourier component of harmonic term, K_1 is a kernel weakly divergent at $u = \pm 1$. s is the instant distance between the tip and the sample and d the closest distance in a cycle of the cantilever oscillation. In order to get a closed form for $F_{\rm ts}(s)$, the kernel K_1 is approximated by the leading divergent term in the vicinity of $u = -1$, $K_1(u) \simeq 1/[2(1+u)]^{1/2}$. The upper

integration range $d + 2A$ can be approximated as infinity for large amplitude limit. The resulting approximated equation is

$$k_{\mathrm{ts}}^{\mathrm{eff}}(d) = \frac{\sqrt{2}}{\pi A^{3/2}} \int_d^{\infty} \frac{F_{\mathrm{ts}}(s)}{\sqrt{s-d}}\,\mathrm{d}s \equiv \boldsymbol{B}(F_{\mathrm{ts}}), \qquad (90)$$

where $\boldsymbol{B}$ is another operator defined here. The inverse operator of $\boldsymbol{B}(F_{\mathrm{ts}})$ is known as [67]

$$F_{\mathrm{ts}} = \boldsymbol{B}^{-1}(k_{\mathrm{ts}}^{\mathrm{eff}}) = -\frac{A^{3/2}}{\sqrt{2}} \int_s^{\infty} \frac{(\mathrm{d}/\mathrm{d}q)k_{\mathrm{ts}}^{\mathrm{eff}}(q)}{\sqrt{q-s}}\,\mathrm{d}q, \qquad (91)$$

where the integration variable d was replaced by q to avoid possible confusion.

By using equation (91), the tip–sample interacting force can be calculated from the experimentally measured frequency shift data k^{eff} as a function of distance. As mentioned previously, this approximation is valid for a cantilever having a large amplitude. Typically, in the case of a micro-machined cantilever, the amplitude A is of the order of 100 nm and the tip–sample force is ∼1 nm. In this case, equation (91) provides a good estimation. However, in the case of the quartz crystal resonator cantilever (e.g. *tuning fork*) [13,16,32] $A \sim 1$ nm, and further correction procedures are required. Dürig calculated the accuracy of his inversion method for the Lennard–Jones type potential ($F_{\mathrm{ts}}(d) = F_0(l^4/3d^6 - 1/d^2)$), where l is a measure of the force range [73]. While for $A \gg l$, equation (91) the equation works very well, for $l < A < 10l$ it yields inaccurate results. As a correction method, he suggested an iterative approach. It starts with the measured frequency shift $k_{\mathrm{ts}}^{\mathrm{eff}}(d) = 2k\Delta f/f_0$ and $\boldsymbol{B}^{-1}$ in equation (91) yields first approximate force F_{ts}^0. By operating $\boldsymbol{A}(F_{\mathrm{ts}}^0)$ in equation (89), one gets the first corrected effective force gradient $k_{\mathrm{ts}}^{\mathrm{eff},0}(d)$. The inaccuracy $k_{\mathrm{ts}}^{\mathrm{eff}}(d) - k_{\mathrm{ts}}^{\mathrm{eff},0}(d)$ is taken as a new argument in the approximate inversion operator $\boldsymbol{B}^{-1}$ to calculate a force correction ΔF_{ts}:

$$\Delta F_{\mathrm{ts}} = \boldsymbol{B}^{-1}(k_{\mathrm{ts}}^{\mathrm{eff}}(d) - k_{\mathrm{ts}}^{\mathrm{eff},0}(d)). \qquad (92)$$

This procedure can be repeated until ΔF_{ts} is reduced within the required accuracy. For the Lennard–Jones type potential, two iterations are enough to achieve 99% accuracy for the large amplitude limit. For $A = l$, 10 iterations give 99% accuracy [73].

6. Atomic imaging

6.1. Atomic image in semiconductor

While the STM unveiled the Si(1 1 1) 7 × 7 structure earlier, a similar image with AFM was obtained by Giessibl with a non-contact AFM in vacuum [35]. Figure 14(*a*) shows a representative FM-AFM image for the Si(1 1 1)- 7 × 7 reconstruction [72]. The set-point of the frequency shift $\Delta f = -28$ Hz, the amplitude $A_0 = 164$ Hz and the scan area $8.9 \times 8.9\,\mathrm{nm}^2$. The unit cell of 7 × 7 structure is guided by solid (faulted) and dashed (unfaulted) triangles. The line profile is shown in figure 14(*b*) along the line in figure 14(*a*). In a unit cell of Si 7 × 7, there are 12 protrusions (adatoms) and

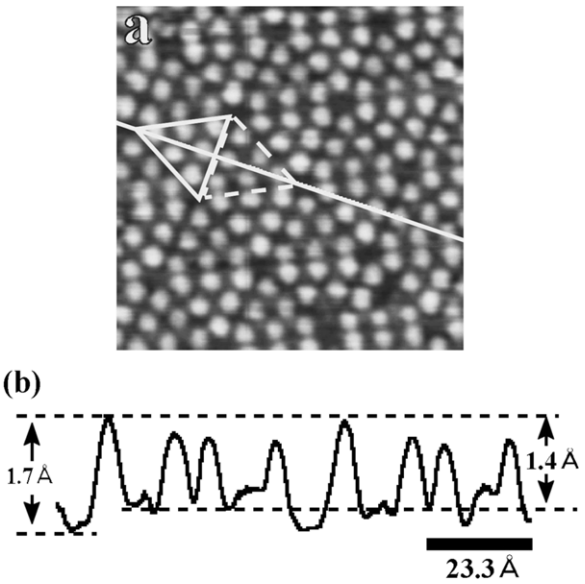

Figure 14. (*a*) FM-AFM image of the Si(1 1 1) 7 × 7 reconstruction. The set-point of the frequency shift is $\Delta f = -28$ Hz, the amplitude $A_0 = 164$ Hz and the scan area $8.9 \times 8.9\,\mathrm{nm}^2$. The unit cell of 7 × 7 structure is guided by solid (faulted) and dashed (unfaulted) triangles. (*b*) The line profile is shown along the line in (*a*). Reprinted figure with permission from [72]. (http://link.aps.org/abstract/PRB/v56/p9834) Copyright (1997) by the American Physical Society.

a deep depression (corner hole). This structure is reconstructed on the surface of Si(1 1 1) due to the spontaneous interactions among Si atoms. The reconstructed structure on the surface is different from the Si crystal structure. The number '7' means the side length of equilateral triangle in figure 14(*a*), in the unit of atomic spacing of the internal crystal structure. The dimer-adatom-stacking fault (DAS) model is generally accepted for an explanation of this structure [74]. The model consists of 12 adatoms arranged locally in the 2 × 2 structure, nine dimers on the sides of the triangular subunits of the 7 × 7 unit cell and a stacking fault layer.

Lantz *et al* [75] measured the force of a chemical bond between Si atoms, quantitatively. The experiment was performed using a low-temperature AFM, a Si tip and a Si (1 1 1) 7 × 7 sample. From the raw data of the force–distance curves on corner hole and adatom, the vdW background force ($F_{\mathrm{vdW}} = -A_{\mathrm{H}}R/6z^2$, where $A_{\mathrm{H}}R = 9.1 \times 10^{-28}$ J m) was eliminated and the short-range chemical bonding force between the adatom in the sample and an atom on the tip was extracted. The force on the adatom estimated from Dürig's inversion procedure was an attractive short-range force with a maximum value of −2.1 nN, which agreed with the first-principle calculation of a covalent bond. With their high resolving power, different interaction potentials from inequivalent adatom sites could be distinguished.

For the III–V semiconductor, Sugawara *et al* [78, 79] imaged the atoms of the InP(110) surface using UHV condition FM-AFM at room temperature. With their UHV AFM, atomic resolution imaging of the cleaved semi-conducting InP(1 1 0) surface was achieved. Also, atomic-scale point defects and motion were observed at room temperature.

Schwarz *et al* [80] reported an atomic-scale study on *in situ* cleaved InAs(1 1 0) using a dynamic mode AFM at low temperatures. The AFM image showed high protrusion on the As atoms, where the valence charge density was at its maximum. Occasionally, the In atoms appeared depending on the tip condition. They observed protrusions as well as depressions at the position of the In atoms. This was attributed to the role of the charge rearrangements induced by the specific electronic structure of the tip. Point defects of As and In atoms were investigated. The observed point defect as a missing protrusion implied the existence of an As vacancy. Another point defect was a vacancy, which was detected indirectly by its influence on two neighboring As atoms.

Recently, Sugimoto *et al* [99] reported a method for chemical identification of individual surface atoms by using force spectroscopy with a home-built FM-AFM. By measuring short-range chemical force for individual atoms at room temperature, they found that the different atoms exert different strengths of chemical forces. An alloy sample was prepared, which was composed of Si, Sn and Pb atoms blended in equal proportions on a Si(1 1 1) substrate. As shown in figures 15(*a*) and (*b*), a topographic image and height distribution of the atoms show that Pb atoms with neighboring Si atoms appear indistinguishable only from their topographic information. However, the force spectroscopic measurement shows a clear discrimination of the atoms. The local chemical composition shown in figure 15(*c*) of the topography was colored by blue, green, and red atoms corresponding to Sn, Pb and Si, respectively, according to the distribution of maximum attractive forces measured by force spectroscopy shown in figure 15(*d*). In order to corroborate their result, a similar measurement was performed on the other region of the sample where some Pb atoms are almost completely surrounded by Si atoms. Figures 15(*e*) and (*f*) show the topographic image and the atomic height distribution histogram. In this case, the Pb atoms are almost indistinguishable from the Si atoms. The force spectroscopy measurement shows unambiguous discrimination of each surface atom, as shown in figure 15(*g*) and (*h*). The image size of figures 15(*a*), (*c*), (*e*) and (*g*) are $4.3 \times 4.3\,\mathrm{nm}^2$.

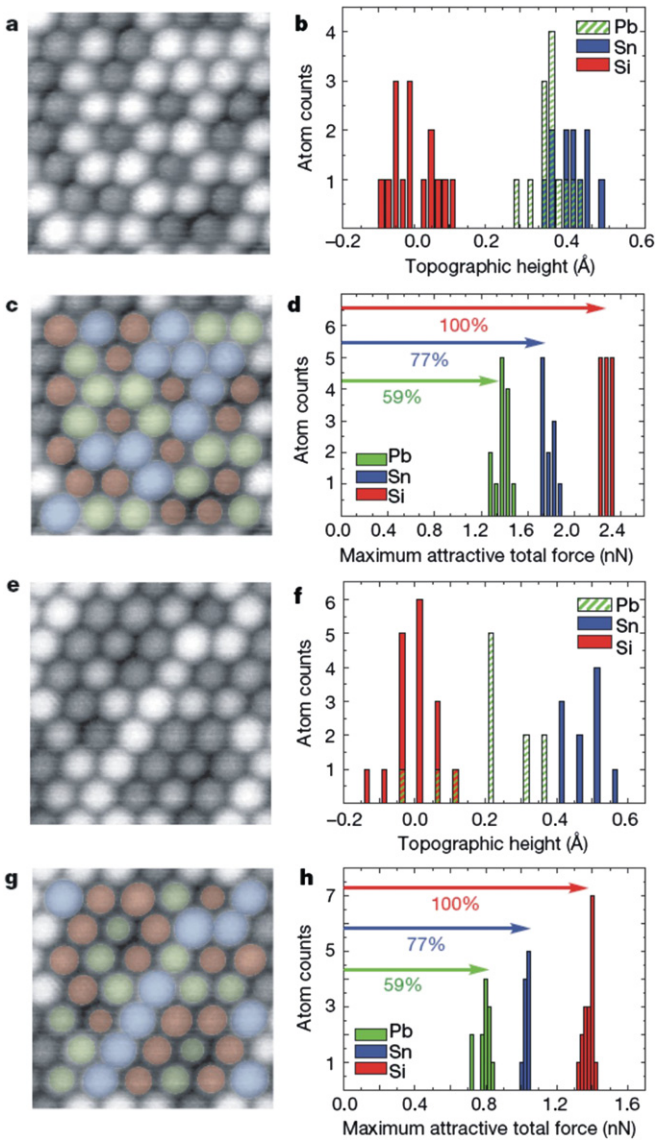

Figure 15. (*a*) Topographic image and (*b*) height distribution of Pb, Sn and Si atoms. The Pb and Sn atoms are indistinguishable from topographic information. (*c*) The local chemical composition was colored by green, blue and red atoms corresponding to Pb, Sn and Si, respectively, and according to (*d*), the distribution of maximum attractive forces measured by force spectroscopy. (*e*) Topographic image and (*f*) height distribution of Pb, Sn and Si atoms are shown. (*g*) The local chemical composition and (h) the distribution of maximum attractive forces show clear segregation of the atoms. The scan size for (*a*), (*c*), (*e*) and (*g*) is $4.3 \times 4.3\,\mathrm{nm}^2$. Reprinted by permission from Macmillan Publishers Ltd: *Nature* [99], copyright (2007).

6.2. *Atomic image in ionic crystal*

Representative ionic crystals include alkali halides and oxides which consist of cation and anion (halogen or oxygen ions). The cation and anions have closed electron shells and attract each other by electrostatic Coulomb force. For the ionic crystal imaging, there is no significant contribution of dangling-bond covalent interaction because of the closed-shell electronic structures of the ions [4]. Therefore, the dominant interacting force yielding the atomic resolution is the electrostatic force exerted by the ions.

Bammerlin *et al* [81] used an FM-AFM with $A_0 = 13\,\mathrm{nm}$ to study alkali halide surfaces. The (0 0 1) cleavage faces of NaF, RbBr, LiF, KI and NaCl were atomically resolved in UHV at room temperature. The observed lattice periods were equal to the bulk lattice constant of equally charged ions. The mean atomic corrugation was comparable to the difference between the anion and cation ionic radii.

Fukui *et al* [82] imaged the TiO_2(1 1 0)-(1 × 1) surface with atomic resolution by FM-AFM in UHV. In contrast to the STM result, outermost atoms of bridge-bound oxygen ridges were observed. With the high resolution imaging, it was found that the bridging oxygen atoms ordered in (1×1) periodicity on terraces. Point defects of oxygen atoms were also imaged as dark spots.

Foster *et al* [83] obtained an atomic resolution image of the CaF_2 (1 1 1) surface with dynamic mode AFM. Both experiments and theory showed a clear triangular pattern. The

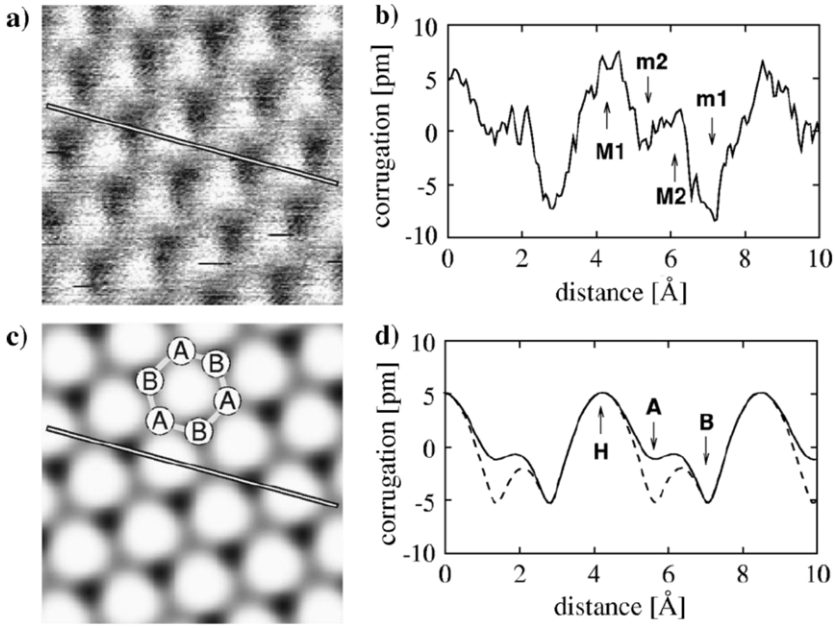

Figure 16. Atomic resolution FM-AFM images of HOPG (0 0 0 1). (*a*) The experimentally obtained images in UHV at $T = 22$ K. (*b*) The line profile of the experimental image along the line in (*a*). (*c*) The theoretically obtained image by using a simulation of the LJ potential. (*d*) The line profile of the simulated image along the line in (*c*). Reprinted figure with permission from [86]. (http://link.aps.org/abstract/PRB/v62/p6967) Copyright (2000) by the American Physical Society.

theory demonstrated that the contrast pattern is caused by the interaction of a positive electrostatic potential tip with fluorine ions in the two topmost layers. They found that the position and the relative height of the line profile measured agreed with theoretical expectations. Their atomic resolution images established unambiguous identification of the sublattices of an insulator.

6.3. Atomic images of HOPG and inert gases

Allers *et al* [84] imaged atoms in highly oriented pyrolytic graphite (HOPG) surface (0 0 0 1) using low-temperature FM-AFM. They pointed out that low-temperature FM-AFM measurements were essential for achieving the required signal to noise ratio for the atomic imaging. At $T = 22$ K, atomic scale structures with 2.46 Å periodicity were found. However, their AFM image showed not a hexagonal but a trigonal structure. Hölscher *et al* [86] explained the discrepancy by simulation using the Lennard–Jones potential shown in figure 16. The measured and simulated atomic resolution image of the HOPG is shown in figures 16(*a*) and (*c*), respectively. The line profiles in figures 16(*b*) and (*d*) show two maxima (M1, M2) and two minima (m1, m2), in which spacing is 1.42 Å. This is the nearest neighbor distance for carbon atoms. The simulation results show that the tip–sample attractive force on the hollow (H) sites at the center of the hexagon is larger than that on the carbon atom sites because the tip interacts with 6 carbon atoms in a hexagon at the hollow site. There are two different atomic sites, A and B in graphite. A site has a nearest neighbor atom in the lower layer, while B site does not. The minima m1 and m2 correspond to the atomic sites B and A, respectively.

The (1 1 1) surface of xenon thin film was studied on the atomic-scale using FM-AFM by Allers *et al* [85]. The solid xenon forms very weakly bound crystal because of inert properties. For this kind of imaging, very stable operating conditions are required. These were implemented at a low-temperature UHV AFM. The atomic image shows sixfold symmetry with 4.35 Å nearest neighbor distance implying the (1 1 1) surface of FCC structure. The measured atomic corrugation of the Xe surface was 25 pm, which is especially large compared with other samples. From theoretical expectation using LJ potential, the corrugation was expected to be 5 pm [4]. Giessibl and Bielefeldt [69] attributed the discrepancy to the elastic deformation of weakly bound Xe atoms in the crystal. In other words, the Xe atoms were pulled to the surface by the tip because of attractive interaction forces.

Some atomic-scale regular patterns were found by static (contact) AFM in ambient conditions. However, this is not a real atomic image, but a collective interaction image of many atoms. Most true atomic resolution images were obtained from a vacuum. Outstanding images among them show detailed features of atomic nature. These were done at low temperatures close to 4.2 K. In early experimental instruments, the optical fiber interferometry method was employed [72, 75, 80, 87–89, 91, 93, 97]. Optical interferometry uses the interference signal between beams emitted from cleaved optical fiber and bounded from cantilever. For this optical alignment, the micro-positioner for fiber translation in 3-dimension and the coarse approach mechanism for tip–sample distance control are required. As a result, the setup is complicated and is not suitable for low temperature (millikelvin temperature) AFM because a large amount of heat is unavoidable.

Recently developed novel tuning fork based AFM has emerged as a candidate for ultra low-temperature AFM [35, 83, 90, 92, 94–96, 98, 99]. Due to the compactness and low power dissipation, the tuning fork is a very

Table 2. List of notable publications regarding high resolution AFM imaging in vacuum and at low temperature.

Author/affiliation	Methods	Sample/features	Year	Reference
Ohta/Hiroshima	Optical fiber	Graphite	1994	[87]
Uchihashi/Osaka	Optical fiber	Si 7 × 7	1997	[72]
Fukui (Iwasawa)/Tokyo	JSPM-4500	TiO_2	1997	[82]
Hug (Guntherodt)/Basel	Optical fiber	NaCl	1999	[88]
Reichling/Freie	Optical fiber	CaF_3	1999	[89]
Schwarz (Wiesendanger)/Hamburg	Optical fiber	InAs	2000	[80]
Giessibl/Augsburg	Tuning fork	Si 7 × 7	2000	[35]
Rychen (Ensslin)/ETH	Tuning fork	Si 7 × 7	2000	[90]
Lantz (Guntherodt)/Basel	Optical fiber	Si 7 × 7	2001	[75]
Foster/College London	Omicron	CaF_2	2001	[83]
Suehira/Osaka	Optical fiber	Si 7 × 7	2001	[91]
Vancura (Ensslin)/ ETH	Tuning fork	2EDG	2003	[92]
Oyabu (Custance)/Osaka	Optical fiber	Si 7 × 7	2003	[93]
Brown (Kane)/Maryland	Tuning fork	100 mK	2004	[94]
Heyde (Freund)/Max-Planck	Tuning fork	NiAl(1 1 0)	2004	[96]
Seo (Chandrasekhar)/Northwestern	Tuning fork	$SrRuO_3$	2005	[95]
Li (Sugawara)/Osaka	Optical fiber	Si(0 0 1)	2006	[97]
Gildemeister/ETH	Tuning fork	100 mK	2007	[98]
Sugimoto (Custance)/Osaka	Optical fiber	Sn/Pb/Si	2007	[99]

promising candidate for future AFM sensors to study quantum phenomena on an atomic scale. The tuning fork is a kind of piezo electric resonator made of quartz having a very high quality factor ($Q = 3000$ in air, it increases by a factor of 10 in vacuum, and 100 at $T = 4.2$ K). In table 2, a list of notable publications regarding high resolution AFM imaging is shown. To improve the AFM resolution and study the quantum nature of nano-structures, recent AFM instruments have a tendency to decrease temperature to 4.2 K. And the tuning fork method has been adapted commonly for millikelvin temperature settings.

7. Summary

Since its invention in 1986 [1], the atomic force microscope (AFM) has been used as an essential tool for studying surface interactions by means of force–distance measurement. A great deal of work has been performed both theoretically and experimentally. The main development of the AFM was assisted by the invention of the micro-machined cantilever. With the advance of MEMS technology, more sophisticated cantilevers with high aspect ratio tip and high Q-value have been developed. Not only optical deflection techniques, but also piezo-electric detection techniques were developed. These include the piezoresistive cantilever methods and the quartz crystal tuning fork method.

When a tip is close to the surface, many different kinds of interacting forces are superposed. The vdW force is exerted on neutral atoms, which is based on the Coulomb interaction. Electrostatic force exists on ionic crystals as well as metallic samples with static charges. Chemical force is a very short-range attractive force originating from chemical interactions forming chemical bonding. Sophisticated AFMs operating in a vacuum and at low temperatures show high resolution images with atomic resolution. This stems from short-range chemical forces or electrostatic forces.

AFM has been employed in a variety of research fields including nano-technology and bio-technology. Since a pioneering work on receptor–ligand bonds studied by Merkel *et al* [11], force spectroscopy has served as an important tool to study biological, physical, chemical and molecular sciences. With static AFM spectroscopy, force–distance curves can be obtained for specific molecules with a functionalized tip. The force–distance curve of the static AFM shows jump-to-contact and jump-off-contact phenomena, which causes a hysteresis loop. From the hysteresis loop, the interacting force strength and distance dependence can be analyzed.

The dynamic AFM uses the resonant nature of the cantilever. One can measure the resonance frequency shift, amplitude and phase. In the case of AM-AFM, the exciting force frequency is fixed and the amplitude and phase are measured. For FM-AFM, the exciting frequency is spontaneously changed following the instantaneous resonance frequency shift, while the amplitude is controlled at a certain value. The simplest model to relate the frequency shift for interacting forces is the harmonic approximation. The harmonic approximation is valid only for long-range forces like magnetic or electrostatic forces. Lee and Jhe's formalism for AM-AFM by using the Laplace transformation provided a rigorous method for the AM force spectroscopy.

Most high resolution AFM images with atomic scales have been obtained by using FM-AFM at UHV and low temperature. The theoretical formalisms for FM-AFM were discussed for small and large amplitudes, separately. The normalized frequency shift γ_{1A} is a good reference point for comparing force strength between the tip and the sample. From experimental data for frequency versus distance, the force–distance curve can be deduced by the inversion procedure suggested by Dürig [73].

Atomic resolution imaging technique has been developed through sophisticated experimental efforts for low-temperature and high-vacuum measurements with dedicated frequency control and detection. The Si(1 1 1) 7 × 7 imaging technique was established as an example for investigating the atomic nature of the sample. Furthermore, the surface physics of ionic crystals and covalent bonding crystals like solid Xe and HOPG

as well as semiconductors have been studied by using the FM-AFM technique.

Conventionally, for low-temperature UHV-AFM, optical fiber interferometry has been employed to detect the cantilever motion located in the low-temperature vacuum chamber. Its complicated instrument and unavoidable excessive heat load, however, make it difficult to apply to millikelvin temperature ranges provided by the dilution refrigerator. Recently, in the effort to reach ultra low-temperature ranges below 4.2 K, tuning fork based AFM has been developed and studied by many pioneering research groups. Due to its advantages, which include compactness and low power dissipation, the tuning fork is a promising candidate for future AFM sensors to study quantum phenomena on an atomic scale.

Acknowledgments

The authors thank M Lee for helpful discussions on formalism for AM-AFM. This work was supported by the National Program for Tera-level Nano-devices of the Ministry of Science and Technology as one of the 21st century Frontier Programs.

References

[1] Binnig G 1986 *US Patent Specification* 4,724,318
[2] Binnig G, Quate C F and Gerber C 1986 *Phys. Rev. Lett.* **56** 930
[3] Cappella B and Dietler G 1999 *Surf. Sci. Rep.* **34** 1
[4] García R and Perez R 2002 *Surf. Sci. Rep.* **47** 197
[5] Giessibl F J 2003 *Rev. Mod. Phys.* **75** 949
[6] Meyer G and Amer N M 1990 *Appl. Phys. Lett.* **57** 2089
[7] Rugar D, Mamin H J and Guethner P 1989 *Appl. Phys. Lett.* **55** 2588
[8] Tortonese M, Barrett R C and Quate C F 1993 *Appl. Phys. Lett.* **62** 834
[9] Albrecht T R, Akamine S, Carver T E and Quate C F 1990 *J. Vac. Sci. Technol.* A **8** 3386
[10] Akamine S, Barrett R C and Quate C F 1990 *Appl. Phys. Lett.* **57** 316
[11] Merkel R, Nassoy R, Leung A, Ritchie K and Evans E 1999 *Nature* **397** 50
[12] Giessibl F J 1998 *Appl. Phys. Lett.* **73** 3956
[13] Giessibl F J, Hembacher S, Bielefeldt H and Mannhart J 2000 *Science* **289** 422
[14] Giessibl F J, Herz M and Mannhart J 2002 *Proc. Natl. Acad. Sci. USA* **99** 12006
[15] Karrai K and Grober R D 1995 *Appl. Phys. Lett.* **66** 1842
[16] Seo Y, Jhe W and Hwang C S 2002 *Appl. Phys. Lett.* **80** 4324
[17] Edwards H, Taylor L, Duncan W and Melmed A J 1997 *J. Appl. Phys.* **82** 980
[18] Israelachvili J 1992 *Intermolecular and Surface Forces* (New York: Academic)
[19] Kittel C 1986 *Introduction to Solid State Physics* 6th edn (New York: Wiley)
[20] Hamaker H C 1937 *Physica* **4** 1058
[21] Giessibl F J 1997 *Phys. Rev.* B **56** 16010
[22] Ohnesorge F and Binnig G 1993 *Science* **260** 1451
[23] Sarid D 1994 *Scanning Force Microscopy* (New York: Oxford University Press)
[24] Olsson L, Lin N, Yakimov V and Erlandsson R 1998 *J. Appl. Phys.* **84** 4060
[25] Law B M and Rieutord F 2002 *Phys. Rev.* B **66** 035402
[26] Giessibl F J and Binnig G 1992 *Ultramicroscopy* **42** 281
[27] Livshits A I, Shluger A L, Rohl A L and Foster A S 1999 *Phys. Rev.* B **59** 2436
[28] Shluger A L, Kantorovich L N, Livshits A I and Gillan M J 1997 *Phys. Rev.* B **56** 15332
[29] Colchero J, Storch A, Luna M, Gomez Herrero J and Baro A M 1998 *Langmuir* **14** 2230
[30] Stifter T, Marti O and Bhushan B 2000 *Phys. Rev.* B **62** 13667
[31] Choe H, Hong M-H, Seo Y, Lee K, Kim G, Cho Y, Ihm J and Jhe W 2005 *Phys. Rev. Lett.* **95** 187801
[32] Seo Y, Choe H and Jhe W 2003 *Appl. Phys. Lett.* **83** 1860
[33] Binnig G, Rohrer H, Gerber Ch and Weibel E 1982 *Phys. Rev. Lett.* **49** 57
[34] Binnig G, Rohrer H, Gerber Ch and Weibel E 1983 *Phys. Rev. Lett.* **50** 120
[35] Giessibl F J 1995 *Science* **267** 68
[36] Jarvis M R, Rérez R and Payne M C 2001 *Phys. Rev. Lett.* **86** 1287
[37] Ohnesorge F M 2000 *Phys. Rev.* B **61** R5121
[38] Manalis S R, Minne S C and Quate C F 1996 *Appl. Phys. Lett.* **68** 871
[39] Minne S C, Manalis S R and Quate C F 1995 *Appl. Phys. Lett.* **67** 3918
[40] Giessibl F J and Trafas B M 1994 *Rev. Sci. Instrum.* **65** 1923
[41] Hao H W, Baro A M and Saenz J J 1991 *J. Vac. Sci. Technol.* B **9** 1323
[42] Gotsmann B, Seidel C, Anczykowski B and Fuchs H 1999 *Phys. Rev.* B **60** 11051
[43] Martin Y, Wiliams C C and Wickramasinghe H K 1987 *J. Appl. Phys.* **61** 4723
[44] Zhong Q, Innis D, Kjoller K and Elings V B 1993 *Surf. Sci. Lett.* **290** L688
[45] Refer to general textbook for introductory mechanics. For example, Marion J B 1970 *Classical Dynamics of Particles and Systems* (New York: Academic)
[46] Cleveland J P, Anczykowski B, Schmid A E and Elings V B 1998 *Appl. Phys. Lett.* **72** 2613
[47] Dürig U, Gimzewski J K and Pohl D W 1986 *Phys. Rev. Lett.* **57** 2403
[48] Sader J E and Jarvis S P 2004 *Appl. Phys. Lett.* **84** 1801
[49] Sader J E, Uchihashi T, Higgins M J, Farrell A, Nakayama Y and Jarvis S P 2005 *Nanotechnology* **16** S94
[50] Lee M and Jhe W 2006 *Phys. Rev. Lett.* **97** 036104
[51] Anczykowski B, Gotsmann B, Fuchs H, Cleveland J P and Elings V B 1999 *Appl. Surf. Sci.* **140** 376
[52] Aime J P, Boisgard R, Nony L and Couturier G 1999 *Phys. Rev. Lett.* **82** 3388
[53] Boisgard R, Michel D and Aime J P 1998 *Surf. Sci.* **401** 199
[54] García R and San Paulo A 1999 *Phys. Rev.* B **60** 4961
[55] Marth M, Maier D, Honerkamp J, Brandsch R and Bar G 1999 *J. Appl. Phys.* **85** 7030
[56] García R and San Paulo A 2000 *Phys. Rev.* B **61** R13381
[57] San Paulo A and García R 2002 *Phys. Rev.* B **66** 041406
[58] Sasaki N, Tsukada M, Tamura R, Abe K and Sato N 1998 *Appl. Phys.* A **66** S287
[59] Hunt J P and Sarid D 1998 *Appl. Phys. Lett.* **72** 2969
[60] Albrecht T R, Grütter P, Horne D and Rugar D 1991 *J. Appl. Phys.* **69** 668
[61] Atia W A and Davis C C 1997 *Appl. Phys. Lett.* **70** 405
[62] Kikukawa A, Hosaka S, Honda Y and Imura R 1994 *Japan. J. Appl. Phys.* **33** L1286
[63] Hölscher H, Allers W, Schwarz U D, Schwarz A and Wiesendanger R 1999 *Appl. Surf. Sci.* **140** 344
[64] Sasaki N and Tsukada M 1998 *Japan. J. Appl. Phys.* **37** L533
[65] Sasaki N and Tsukada M 1999 *Appl. Surf. Sci.* **140** 339
[66] Dürig U 1999 *Appl. Phys. Lett.* **75** 433
[67] Dürig U 2000 *New J. Phys.* **2** 5

[68] Livshits A, Shluger A and Rohl A 1999 *Appl. Surf. Sci.* **140** 327
[69] Giessibl F J and Bielefeldt H 2000 *Phys. Rev.* B **61** 9968
[70] Ke S H, Uda T and Terakura K 1999 *Phys. Rev.* B **59** 13267
[71] Guggisberg M, Bammerlin M, Loppacher Ch, Pfeiffer O, Abdurixit A, Barwich V, Bennewitz R, Baratoff A, Meyer E and Guntherodt H-J 2000 *Phys. Rev.* B **61** 11151
[72] Uchihashi T, Sugawara Y, Tsukamoto T, Ohta M, Morita S and Suzuki M 1997 *Phys. Rev.* B **56** 9834
[73] Dürig U 2000 *Appl. Phys. Lett.* **76** 1203
[74] Takayanagi K, Tanishiro Y, Takahashi M and Takahashi S 1985 *J. Vac. Sci. Technol.* A **3** 1502
[75] Lantz M A, Hug H J, Hoffmann R, van Schendel P J A, Kappenberger P, Martin S, Baratoff A and Güntherodt H-J 2001 *Science* **291** 2580
[76] Herz M, Giessibl F J and Mannhart J 2003 *Phys. Rev.* B **68** 045301
[77] Holscher H, Gotsmann B, Allers W, Schwarz U D, Fuchs H and Wiesendanger R 2001 *Phys. Rev.* B **64** 075402
[78] Sugawara Y, Ohta M, Ueyama H and Morita S 1995 *Science* **270** 1646
[79] Sugawara Y, Ohta M, Ueyama H, Morita S, Osaka F, Ohkouchi S, Suzuki M and Mishima S 1996 *J. Vac. Sci. Technol.* B **14** 953
[80] Schwarz A, Allers W, Schwarz U D and Wiesendanger R 2000 *Phys. Rev.* B **61** 2837
[81] Bammerlin M, Lüthi R, Meyer E, Baratoff A, Lü J, Guggisberg M, Loppacher C, Gerber C and Güntherodt H-J 1998 *Appl. Phys.* A **66** s293
[82] Fukui K, Onishi H and Iwasawa Y 1997 *Phys. Rev. Lett.* **79** 4202
[83] Foster A S, Barth C, Shluger A L and Reichling M 2001 *Phys. Rev. Lett.* **86** 2373
[84] Allers W, Schwarz A, Schwarz U D and Wiesendanger R 1999 *Appl. Surf. Sci.* **140** 247
[85] Allers W, Schwarz A, Schwarz U D and Wiesendanger R 1999 *Europhys. Lett.* **48** 276
[86] Hölscher H, Allers W, Schwarz U D, Schwarz A and Wiesendanger R 2000 *Phys. Rev.* B **62** 6967
[87] Ohta M, Sugawara Y, Morita S, Nagaoka H, Mishima S and Okada T 1993 *J. Vac. Sci. Technol.* B **12** 1705
[88] Hug H J, Stiefel B, van Schendel P J A, Moser A, Martin S and Güntherodt H-J 1999 *Rev. Sci. Instrum.* **70** 3625
[89] Reichling M and Barth C 1999 *Phys. Rev. Lett.* **83** 768
[90] Rychen J, Ihn T, Studerus P, Herrmann A, Ensslin K, Hug H J, van Schendel P J A and Güntherodt H-J 2000 *Appl. Surf. Sci.* **157** 290
[91] Suehira N, Tomiyoshi Y, Sugawara Y and Morita S 2001 *Rev. Sci. Instrum.* **72** 2971
[92] Vancura T, Kicin S, Ihn T, Ensslin K, Bichler M and Wegscheider W 2003 *Appl. Phys. Lett.* **83** 2602
[93] Oyabu N, Custance O, Yi I, Sugawara Y and Morita S 2003 *Phys. Rev. Lett.* **90** 176102
[94] Brown K R, Sun L and Kane B E 2004 *Rev. Sci. Instrum.* **75** 2029
[95] Seo Y, Cadden-Zimansky P and Chandrasekhar V 2005 *Appl. Phys. Lett.* **82** 103103
[96] Heyde M, Kulawik M, Rust H-P and Freund H-J 2006 *Phys. Rev.* B **73** 125320
[97] Li Y J, Nomura H, Ozaki N, Naitoh Y, Kageshima M and Sugawara Y 2006 *Phys. Rev. Lett.* **96** 106104
[98] Gildemeister A E, Ihn T, Barengo C, Studerus P and Ensslin K 2007 *Rev. Sci. Instrum.* **78** 013704
[99] Sugimoto Y, Pou P, Abe M, Jelinek P, Perez R, Morita S and Custance O 2007 *Nature* **446** 64